TÉCNICO LISBOA

Frequency resolved optical gating for ultrashort mid-infrared laser pulses

Luís de Gonzaga Ferin de Melo da Cunha Veloso

Thesis to obtain the Master of Science Degree in

Engineering Physics

Supervisors: Prof. Hugo Filipe de Almeida Pires
Prof. Gonçalo Nuno Marmelo Foito Figueira

Examination Committee

Chairperson: Prof. João Alberto dos Santos Mendanha Dias
Supervisor: Prof. Gonçalo Nuno Marmelo Foito Figueira
Members of the Committee: Prof. Celso Manuel de Figueiredo Paiva João
Prof. Paulo Sérgio De Brito André

December 2021

Acknowledgments

First and foremost I would like to express my sincerest gratitude to my supervisors. Thank you Prof. Gonçalo Figueira for the opportunity, and patience which made this thesis possible. Very special thanks particularly to Prof. Hugo Pires for his invaluable support and patience, and for always being so reachable. Thank you so much. Thank you also to Joana Alves for her help in the Laboratory for Intense Lasers, and to my colleague Gonçalo Vaz.

I would like to extend my thanks also to the faculty, Instituto Superior Técnico, for all its learning opportunities and, especially, its lesson in perseverance.

Reaching the conclusion of my studies, I cannot help but to thank all the people who made me grow until now.

Many thanks, then, first, to my family. In particular, to my late mother, Mafalda Maria Ribeiro Ferin-Cunha for her motherly love made evident specially when helping me study everyday after school when I was struggling. To my father, Luís Manuel de Magalhães de Albuquerque Veloso for the unparalleled formation opportunities and persistence in raising me. To my eldest brother Afonso Lázaro Ferin-Cunha de Albuquerque Corte-Real for always setting a standard of excellence for me to strive for. To my brother Manuel José Ferin-Cunha de Magalhães e Albuquerque for his testimony of a joyous and ordered life. To my dearest cousin, Ana Carlota Ferin-Cunha de Bragança Balula Cid for always welcoming me into her family, and helping me not lose sight of the essential in life.

To all my friends, thank you for sharing, not just the fun, but most importantly, the challenges of life with me. Special thanks to Afonso Freitas do Amaral Cardoso da Silva for his loyalty and kindness beyond words.

J. R. R. Tolkien once wrote to his son a letter saying: “Out of the darkness of my life, so much frustrated, I put before you the one great thing to love on earth: the Blessed Sacrament... There you will find romance, glory, honour, fidelity, and the true way of all your loves upon earth.” The greatest thanks then to the Catholic Church, in all its consecrated and lay members, for passing on the gift of faith.

I am but a fool who only made it this far because all of you wouldn’t give up on me. For that, my deepest, sincerest thanks, and a pledge to pass on, to the best of my ability, what each of you has selflessly given me.

AMDG

Resumo

A expansão do conjunto de aplicações de impulsos lasers ultracurtos levou nas últimas décadas os investigadores a empenharem-se em obter impulsos a cada vez mais curtos. Uma consequência disso são os desafios na sua medição quando não há outro impulso mais curto com o qual compará-lo. A técnica FROG, apresentada pela primeira vez em 1991, é capaz de caracterizar estes impulsos. Mas o desenvolvimento na última década de pulsos ultracurtos no infravermelho médio levantou outros desafios na sua medição devido às dificuldades inerentes à manipulação de feixes nesse comprimento de onda.

Neste trabalho, desenvolvemos um diagnostico FROG para pulsos ultracurtos no infravermelho médio. Em particular, comparamos e aplicamos um algoritmo de ponta baseado em pticografia com um algoritmo tradicional para obter uma precisão superior em pulsos complexos. Para enfrentar as dificuldades do infravermelho médio no processo de geração de segunda harmónica (SHG), usamos um crystal $AgGaS_2$. Assim, caracterizamos dois impulsos lasers de 1 µm, um oscilador e um de alta potência usando a técnica FROG, e um impulso de um laser OPCPA de 3 µm usando o método da autocorrelação.

Conhecer o comprimento de um impulso laser é o alicerce sobre o qual a investigação em óptica é desenvolvida.

Keywords: Infravermelho-médio, laser, ultracurto, FROG, SHG, pticografia

Abstract

The broadening set of applications of ultrashort laser pulses has driven researchers in the past decades to continuously push through to obtain shorter and shorter pulses. One shortcoming of this are the challenges in their measurement if there is no other shorter pulse available to compare it with. The FROG technique, first presented in 1991, is capable of characterizing these pulses. But the development in the past decade of ultrashort pulses in the mid-infrared raises new challenges in their measurement due to the inherent difficulties in the manipulation of beams in said wavelength range.

In this work, we develop a FROG diagnostic for ultrashort pulses in the mid-infrared. In particular, we benchmark and use a state of the art ptychography based algorithm against a traditional one to achieve superior precision in complex pulses. To tackle the difficulties of the mid-infrared region in the SHG process, we use a $AgGaS_2$ crystal. We thus characterize two 1 µm laser pulses, an oscillator and a high power one using FROG, and a 3 µm OPCPA laser pulse using the autocorrelation method.

Knowing the pulse length is the foundation on which future research in optics in this laboratory is built.

Keywords: Mid-infrared, ultrashort, laser, FROG, SHG, ptychography

Contents

List of Tables

List of Figures

Chapter 1

Introduction

Ever since their invention in 1960, lasers have found applications in numerous fields, ranging from research, to everyday use, from the detection of gravitational waves, to DVD players. Indeed, in addition to the multiple laser related Nobel prizes, more than fifty-five thousand patents involving the laser have been granted in the United States alone, averaging at about three per day [1]. Driven by the broadening set of applications made available by their existence, researchers are continuously pushing through to obtain shorter and shorter laser pulses. Figure 1.1 presents the evolution of the shortest developed pulse duration over time. From the probing of ultrafast physical, chemical and biological processes [1], to ultrafast optical fiber communications, ultrashort laser pulses progressively unlock new possibilities.

However, it is of little use to strive for ever shorter laser pulses if we are not able to measure them. This measurement goes beyond the issue of temporal length alone, but also involves the pulse structure and phase. In this work, we aim to determine those characteristics for the newly installed laser system in the Laboratory for Intense Lasers , at Instituto Superior Técnico .

1.1 Objectives and methods

1.1.1 The challenges

The emergence of ultrashort laser pulses in the range of only a few femtoseconds (10^{-15} s) has brought a number of new challenges to this field. To measure a certain event, we must use shorter ones; for instance, a stopwatch is used to measure the speed of an athlete, a camera with a fast shutter to capture a bird flapping its wings... But how can we measure the shortest events ever created? There is no shorter event to compare it with. We somehow have to make do with the second best thing: the pulse itself.

Manipulating ultrashort pulses also has its difficulties. Most noteworthy of all is that extremely large bandwidths have to be handled, from tens to hundreds of nm. Indeed, to process an ultrashort pulse, special attention must be paid to the choice of materials used in the optical system to ensure that they can accommodate the desired optical processes without losses, distortions or excessive dispersion. For instance, in this work, the Frequency-Resolved Optical Gating (FROG) technique mixes two signals in a non-linear medium to form a third one, be it through second - or third - harmonic generation, a polarization gate, etc... Regardless, the materials should be able to carry out their intended purpose, as best as possible, without altering the pulse itself or distorting the desired information.

The past decade has witnessed the emergence in particular of ultrashort laser systems in the mid-infrared spectral range (2-10 µm). In this region, the above listed problems become even more evident

[1] LaserFest — Early History. URL: http://laserfest.org/lasers/history/early.cfm (visited on 01/08/2021).

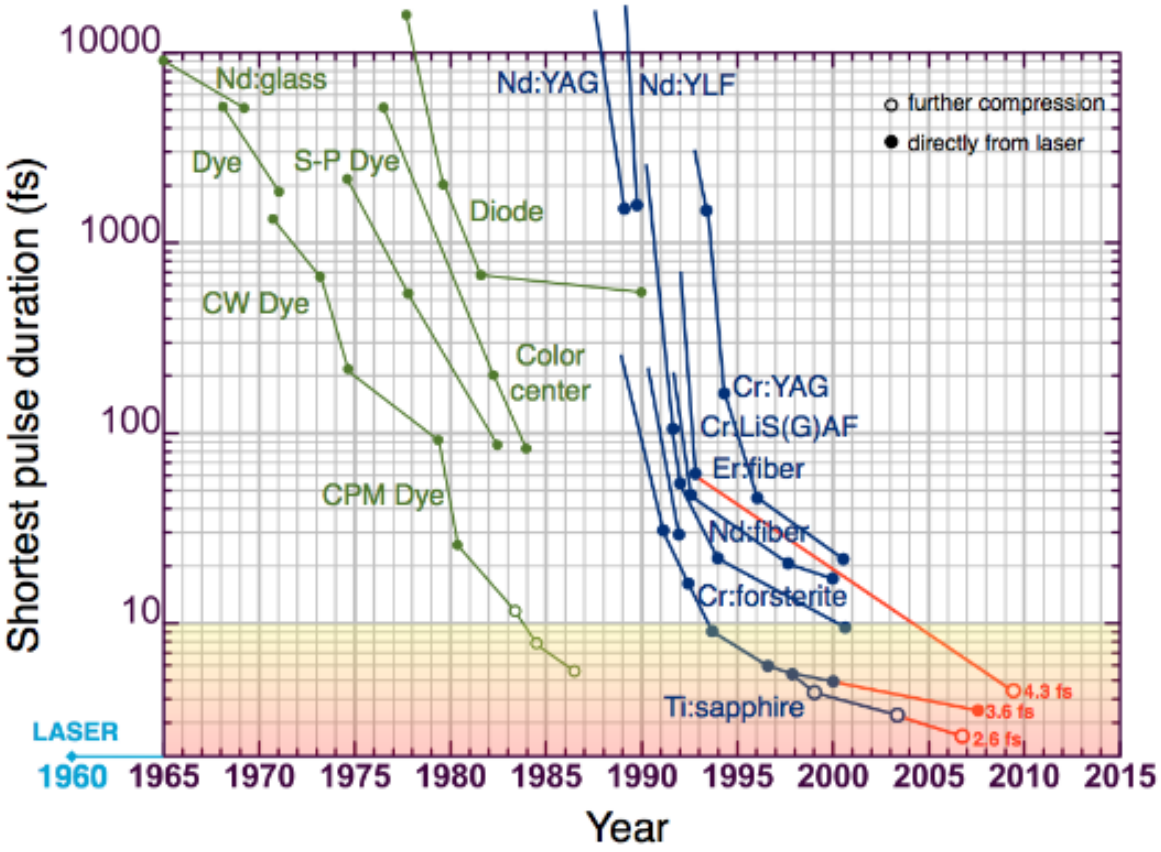

Figure 1.1: Evolution of shortest pulse duration. © Alexandra A. Amorim, FCUP

due to the lack of suitable equipment and the bandwidth being even broader. Note that, for a 100 fs pulse, the bandwidth (in wavelength range) is around 20 times larger at 3000 nm than at 650 nm. The materials must then be validated for operation in the full wavelength range of our laser pulses.

1.1.2 Our goal

Pulse retrieval techniques in the near-infrared - such as FROG or Electro-Optic Sampling [2] - have already been explored for a while now and several diagnostic devices are commercially available. It is also the case of mid-infrared pulses despite them being more recent. However, given the expensive cost of these devices and the fact that the host research group has the necessary know-how and equipment, it was decided to design, build, test and demonstrate this device using our own resources, which is the main content of the work described in this thesis.

The ultimate goal to achieve with this work is full temporal characterization of the laser pulses of the novel 3 µm OPCPA (Optical parametric chirped-pulse amplification) Fastlite laser system. Below we provide the main steps required to retrieve that information.

1.2 State of the art

1.2.1 Pulse measurement

When we talk about measuring a pulse, we actually mean determining its electric field as a function of time and/or space. Assuming that the spatial and temporal quantities are independent we can write the (real) electric field as a function of time as:

$$\mathcal{E}(t) = \frac{1}{2}\sqrt{I(t)}\exp\{i[\omega_0 t - \phi(t)]\} + c.c., \tag{1.1}$$

where t is the time in the reference frame of the pulse, ω_0 is a carrier angular frequency, and $I(t)$ and $\phi(t)$ are the pulse intensity and temporal phase. The complex conjugate (c.c.) is necessary to make the pulse real, but can be ignored to simplify the calculations and added back at any time. Usually, we wish to obtain the pulse complex amplitude:

$$E(t) = \sqrt{I(t)}\exp[-i\phi(t)] \tag{1.2}$$

Fourier transforming this to the frequency domain, we have:

$$\widetilde{E}(\omega) = \sqrt{S(\omega)}\exp[-i\varphi(\omega)] \tag{1.3}$$

where $S(\omega)$ is the spectral intensity (also called "the spectrum") and $\varphi(\omega)$ is the spectral phase. And so, the pulse duration that we are looking for is actually the FWHM of the temporal intensity, $I(t)$.

In terms of pulse lengths, it is common practice to classify as "ultrashort" those pulses not exceeding a few hundreds of femtoseconds, although this limit has become shorter over the years. Figure 1.2 shows the electric field and related concepts for an example pulse.

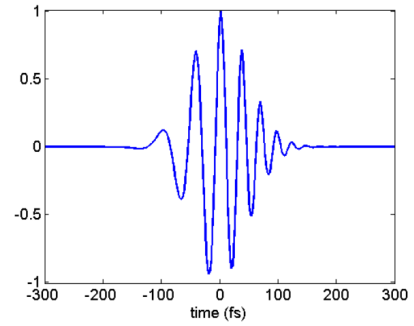

(a) The real part if $E(t)$

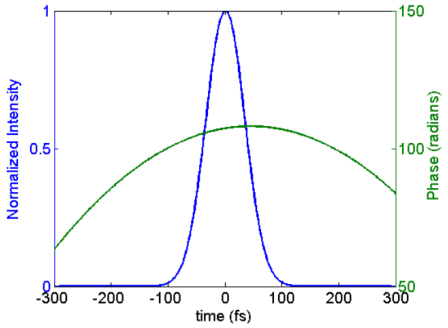

(b) The intensity and phase of $E(t)$

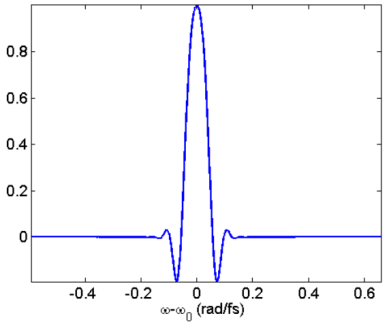

(c) The real part if $E(\omega - \omega_0)$

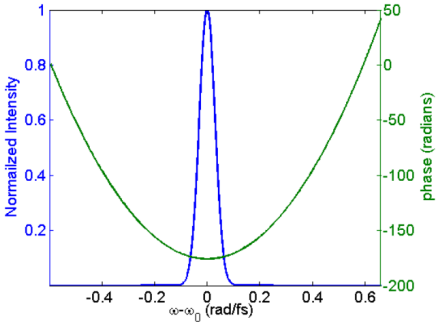

(d) The intensity and phase of $E(\omega - \omega_0)$

Figure 1.2: Plotting the complex electric field of an ultrashort pulse [3]

Generally, when we wish to measure a pulse, there are two things that we need to take into consideration to have a trustworthy result. First, the technique must be capable of determining complex pulses as well as simple pulses. Should it be unable to measure the former, all the pulses will appear as simple ones because it is the only thing it can find. Second, a device typically averages over many possible pulses and provides a single solution, so we need some sort of mechanism that tells us how well the device's output resembles the actual pulse.

1.2.2 The one dimensional phase-retrieval problem

The spectrum $S(\omega)$ has been the most straightforward of these quantities to obtain. A form of spectrometer has a beam directed on to a diffraction grating, and the resulting dispersed beam is imaged on a camera. Another technique uses an interferometer to obtain the light's field autocorrelation:

$$\Gamma^{(2)}(\tau) = \int_{-\infty}^{\infty} E(t)E^*(t-\tau)\,dt \tag{1.4}$$

The autocorrelation theorem states that:

$$|\widetilde{E}(\omega)|^2 = \mathcal{F}\left\{\int_{-\infty}^{\infty} E(t)E^*(t-\tau)\,dt\right\} \tag{1.5}$$

which, comparing with equation 1.3, is simply the spectrum.

However, to fully characterize a pulse, it is necessary to have the intensity and the phase in any of the two domains (time or frequency). This problem is called the one-dimensional phase-retrieval problem. As it turns out, we do not have enough constraints to uniquely determine the phase. There are, for starters, the "trivial" ambiguities. If we have a certain spectrum for a pulse of electric field $E(t)$, adding a constant phase shift $E(t)\exp(i\phi_0)$ will not change its spectrum, as we can see in equation 1.5. The same goes for a time translation $E(t-t_0)$, and a time reversal $E^*(-t)$. But besides these ambiguities, there are other much more problematic ones. Although the condition that the pulse asymptotes to 0 as $t \to \infty$ is quite powerful, it is not enough to remove these "non-trivial" ambiguities. Akutowicz showed in two papers written in 1956 and 1957 that there is an infinity of such pulse fields that satisfy these constraints. [4, 5]

1.2.3 The intensity autocorrelation

The first technique developed to measure laser pulses dates back to the 1960's. To measure a continuous quantity in two dimensions, several discrete measurements have to be made to trace an approximate profile of the function. The shorter the interval between those measurements, the more precise is the trace. In optics, this is done using a gating function (or signal), where the measurement is made during a short time interval. By repeating this measurement in all the portions of the pulse, we obtain a signal that is proportional to the area under the transmitted pulse. Now, to operate this gate, electronic devices are too slow, so a shorter laser pulse plays the role of the gate. This gating phenomenon can be achieved e.g. by using a pulse mixing nonlinear process such as second harmonic generation. The two pulses are overlapped in a nonlinear medium, creating a third pulse that is then detected by the camera. Imparting a controllable delay on to the gating pulse will allow obtaining the range of measurements necessary to reconstruct the pulse. As the (electronic) detectors are too slow, it is the integral over time that is retrieved. The measured photocurrent will then be:

$$i_p(t) \propto \int I(\tau)W(t-\tau)\,d\tau, \tag{1.6}$$

where $W(t)$ is the gating function and τ is the delay. Figure 1.3 illustrates this concept.

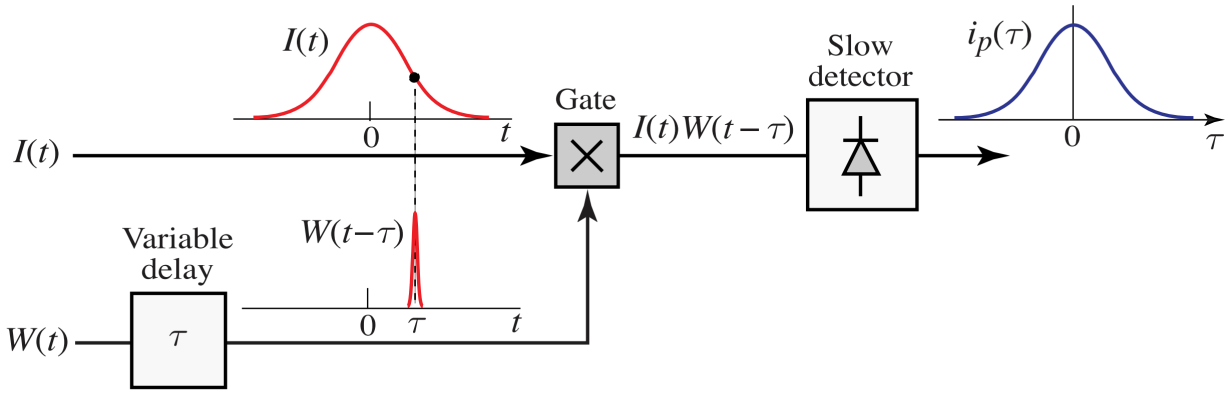

Figure 1.3: Schematic of the concept behind the technique for measuring an optical pulse by use of an optical gate [1, p. 1147]. The gating function $W(t)$ is delayed and then operates the gate to retrieve, with the detector, the portion corresponding to that delay of the initial pulse $I(t)$. Repeating the measurement for all portions of the initial pulse allows to reconstruct the pulse.

We now face the problem that no shorter pulse is available for our gating function. In this case the pulse is used to gate itself. The photocurrent measured will then be proportional to the intensity autocorrelation:

$$A^{(2)}(\tau) = \int_{-\infty}^{\infty} I(t)I(t-\tau)\,dt. \tag{1.7}$$

Applying the Autocorrelation Theorem to Eq. 1.7, we get

$$\widetilde{A}^{(2)}(\tau) = |\widetilde{I}(\omega)|^2. \tag{1.8}$$

We then have the magnitude of the quantity that we want, $I(t)$. Figure 1.4 shows a diagram of a generic autocorrelator. However, we are still lacking the phase. We are facing here again the one dimensional phase-retrieval problem. The autocorrelation then necessarily suffers from the non-trivial amiguities as well as the trivial ones. But there are now better constraints. As equation 1.8 shows, $I(t)$ is real as well as non-negative. Moreover, the goal is more modest, as we only want the intensity, not the entire field.

Nevertheless, despite all the variations of the autocorrelation technique developed to reduce the number of ambiguities, the one-dimensional phase-retrieval problem was never solved. Yet, this technique allows for rough estimations of pulse length. However, it involves making a guess as to the pulse shape: Gaussian, Lorenztian, sech^2 and so on. We can then derive analytically a multiplicative factor relating the widths of the autocorrelation function and the original pulse. This allowed researchers to progress until the 1980's, when the necessity of the phase became more severe than ever to push forward.

1.2.4 The time-frequency domain

In 1991 [7][8] a new approach was considered, consisting in obtaining a frequency resolved autocorrelation, i.e. measuring the delay-dependent pulse spectrum rather than just its intensity. This results in a new domain of operation: the time-frequency domain. The mathematical description of this is the

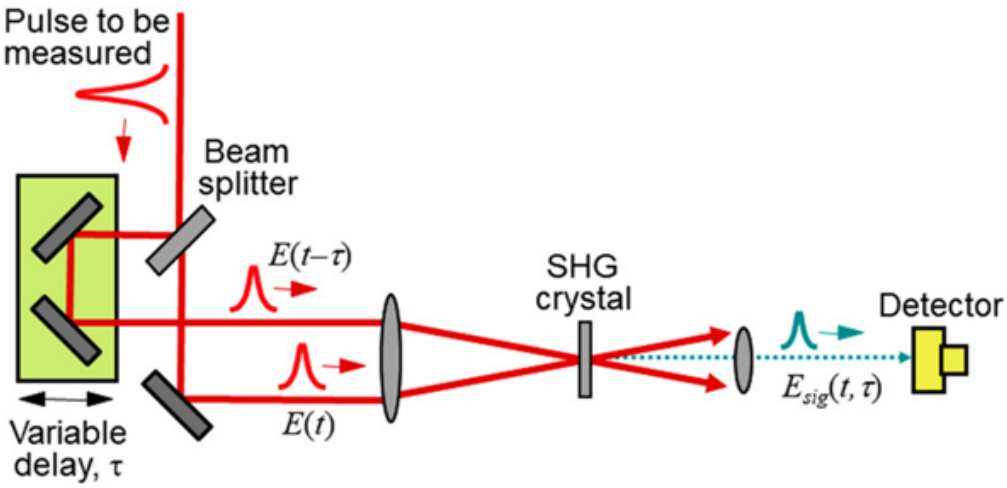

Figure 1.4: Autocorrelator setup [6, p. 4]. The initial beam is split in two in the beamsplitter. One of the beams is delayed, before recombining both in the SHG crystal. The detector captures the portion of the autocorrelation corresponding to that delay.

spectrogram (a.k.a. ”trace”):

$$\Sigma_g(\omega,\tau) = \left| \int_{-\infty}^{\infty} E(t) g(t-\tau) \exp(-i\omega t)\, dt \right|^2 \tag{1.9}$$

This is the Fourier transform of a gated pulse, where $g(t-\tau)$ is a gate function with variable delay; the spectrogram is then a two-dimensional representation of the wave form as a function of the frequency and the delay. Figure 1.5 shows some examples of spectrogram traces, and figure 1.6 shows a more detailed one. This is called the frequency resolved optical gating (FROG) technique. A useful characteristic of this trace is that we can still recover the information of the autocorrelation by simply integrating the signal in frequency. However, we now face the two-dimensional phase-retrieval problem.

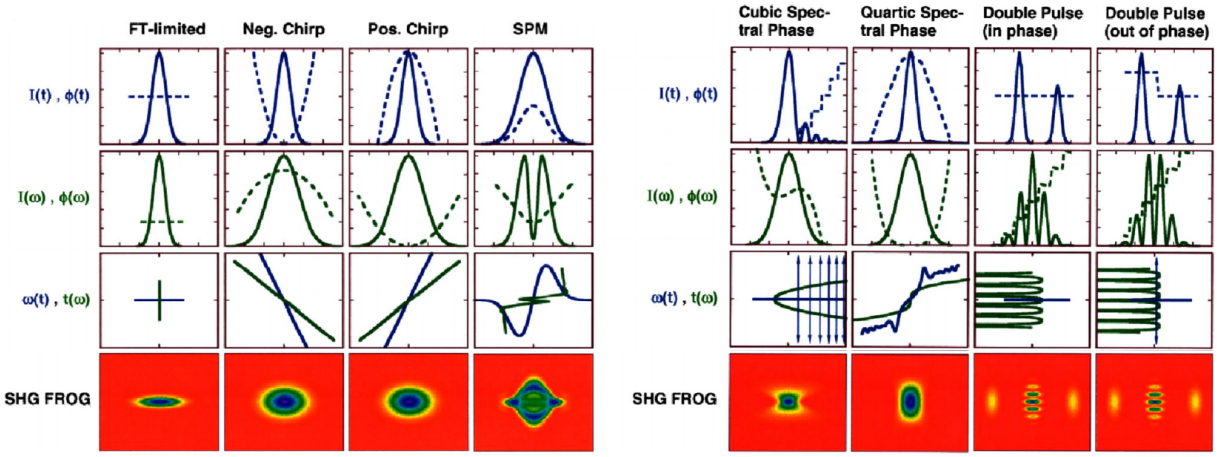

Figure 1.5: FROG traces for common ultrashort-pulse distortions [9, p. 55-56]. Each column shows a different pulse example. The first line shows the time dependent intensity and phase for a given pulse; the second, the frequency dependent intensity and phase; the third, the phase vs time and time vs phase; the final line represents the spectrogram.

Surprisingly, by complicating the problem, it can now be solved, thus yielding a unique solution for the pulse. This results from the fact that the Fundamental Theorem of Algebra, whose polynomial factorization holds for one dimension yielding infinite solutions, but fails in two dimensions. Only the

trivial ambiguities persist.

Also, a very strong constraint can now be used, regarding the mathematical form that the nonlinear optical signal field issued from SHG crystal can have: $E_{sig}(t,\tau) = E(t)E(t-\tau)$. With this additional restraint, the problem is solved, as we shall see further on.

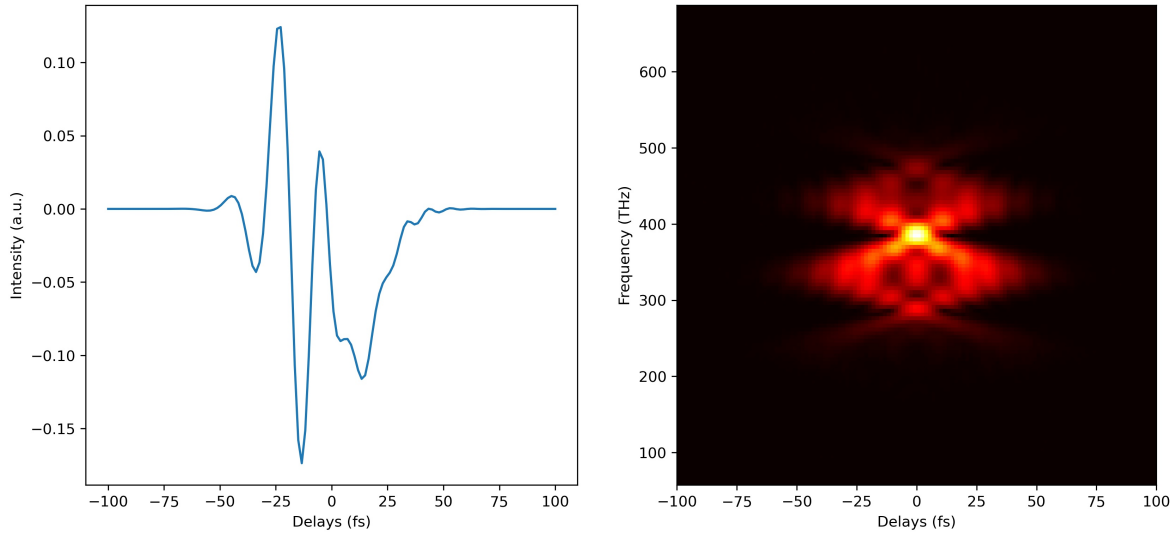

Figure 1.6: Example pulse electric field (left) and respective spectrogram (right) from the ptychographic algorithm pulse bank [10]

We have finally reached the technique that we needed, one able to measure the shortest event created without the need of a shorter one. Interestingly, this technique actually would not work if we had a delta function gating pulse. Substituting $g(t-\tau)$ in equation 1.9 with a such a function would yield only the pulse intensity in function of time, leaving out the phase, what we were looking for in the first place.

1.2.5 FROG algorithms

We now come to the final stage of the work: decoding the FROG trace to obtain the actual pulse length and shape. For that, we need a FROG retrieval algorithm.

This kind of algorithm is an iterative one and there are many different versions. In a generic FROG algorithm (Figure 1.7) the starting point is making an initial guess for the E-field $E(t)$. A signal of the field $E_{sig}(t,\tau)$ is generated, which is then Fourier transformed to obtain the spectrogram $E_{sig}(\omega,\tau)$. At this point the measured trace is compared with our field in the spectral domain. The trace in the time-frequency domain is then used to improve the estimation. This is done by comparing and adjusting the magnitudes of $|E_{sig}(\omega,\tau)|^2$ as it should be equal to $I_{FROG}(\omega,\tau)$. This corrected field is then inverse transformed back into the time domain. Finally, a new guess for the electric field is generated to repeat the process. Ideally, each new guess is better than the previous one and the method converges into the true field.

There is one algorithm however that has proven itself capable of retrieving virtually every pulse: the generalized projections (GP) algorithm [6, p. 14]. Its operation principle is illustrated in figure 1.8. From the initial guess, the trace will correct it, in the frequency domain, to the closest point that satisfies the data constraint. A new projection is then made, in the time domain, to the closest point that satisfies the mathematical-form constraints. For simple pulses, this algorithm converges 75% of the time in the presence of noise on the first guess. For very complicated pulses in the presence of noise, convergence occurs about half of the time.

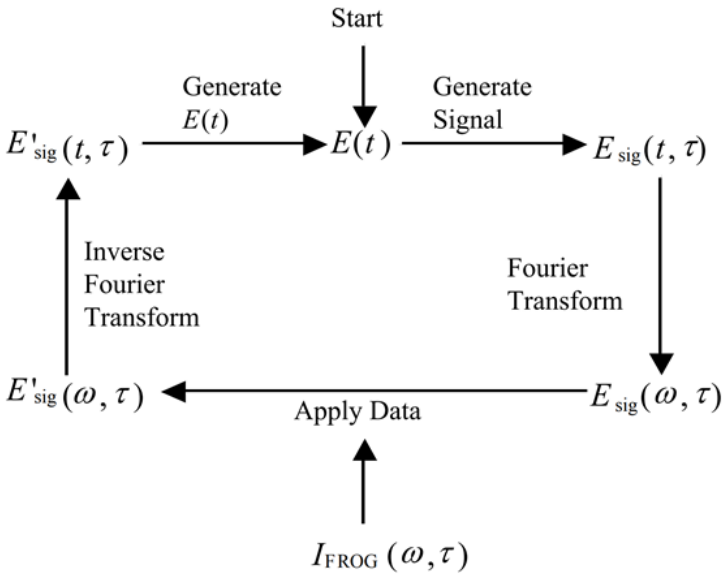

Figure 1.7: FROG generic algorithm diagram [9, p. 71].

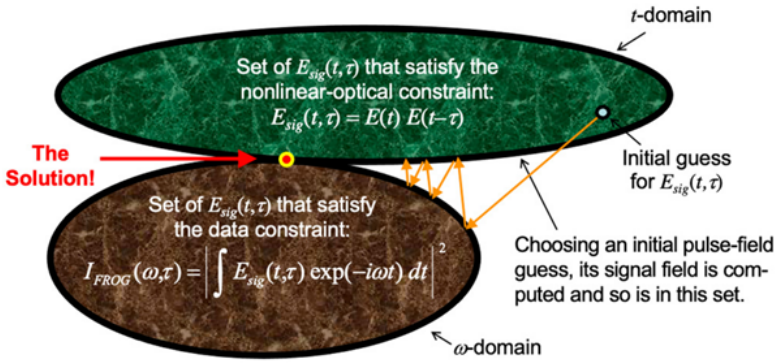

Figure 1.8: Generalized projections algorithm [6, p. 14].

When the algorithm fails to converge, it can be re-run with a different guess. But an algorithm has recently been developed that converges 100% of the time, even for complicated pulses: the Retrieved Amplitude N-grid Algorithm (RANA) [11][12][13]. It generates guesses until the GP converges, and each try is faster than a normal GP algorithm. This is in part because the guess is much better; it uses the spectrum of the signal, simply obtained by integrating the FROG trace in time.

Despite its efficiency in retrieving pulses, this GP-based algorithm presents multiple restricting factors that do not allow to fully exploit the FROG technique's power. In 2016, a new method based on ptychography was introduced [10]. It outperformed previous algorithms in terms of robustness to noise and speed. Indeed, the algorithm can successfully recover pulses with fewer measurements than competing techniques. The comparison simulation in figure 1.9 shows the reliability of the ptychographic algorithm.

The algorithm starts by discretizing the trace $I^{SHG}_{FROG}(\omega,\tau)$ into J values $I_j(\omega)$ with $j = 1\ldots J$, each associated to a certain delay, but in a random order. The ptychographic algorithm then works in one dimension as opposed to the other algorithms, which work in a two-dimensional trace. Each iteration of the algorithm runs through the J spectra and tries to find the signal $E(t)$ that produced it. The iterations continue until the difference between the measured and calculated FROG traces is smaller than the

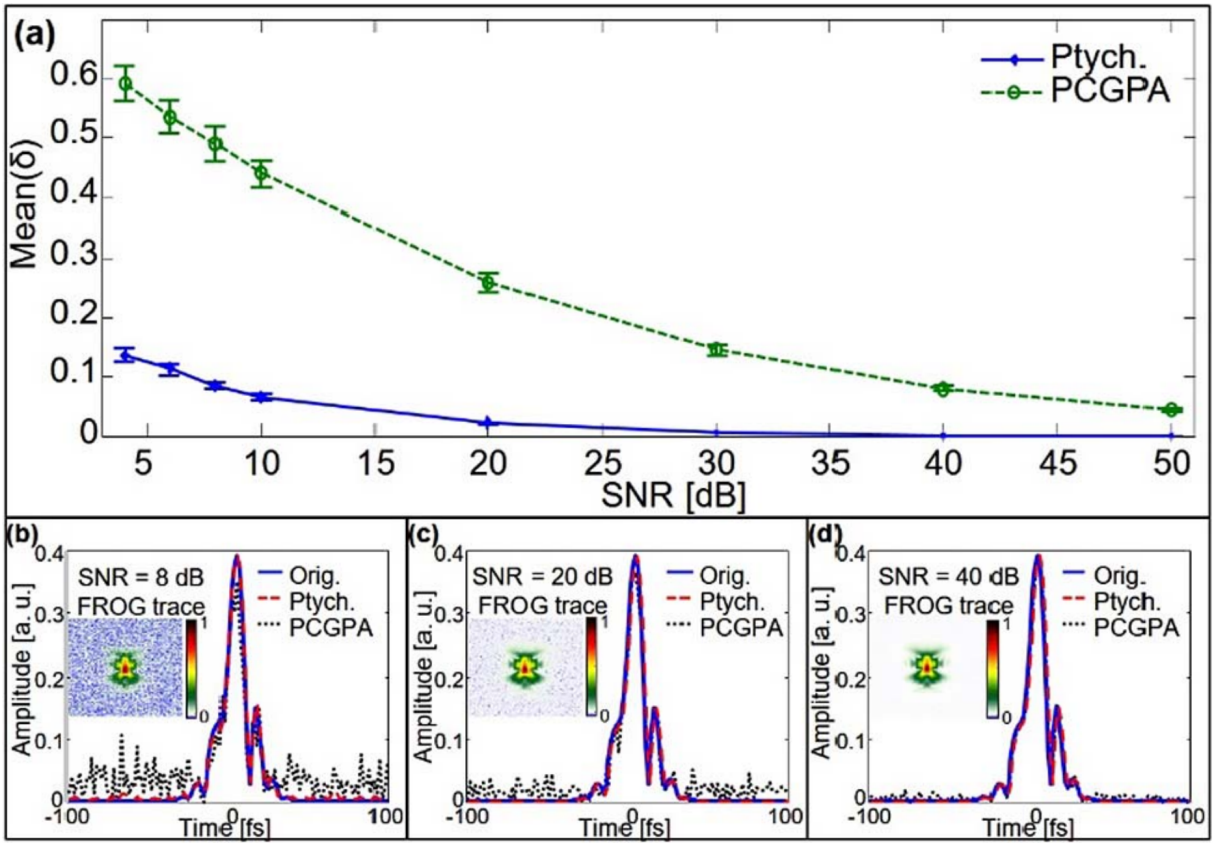

Figure 1.9: Comparison of an improved GP algorighm, PCGPA (Principal Components Generalized Projections Algorithm [8]) with the ptychographic one for different SNR values. (a) The mean angle δ between reconstructed and true signals as a function of the SNR represents the error. Plots (b)–(d) show a true pulse reconstructed by both algorithms with varying SNR. [10]

signal to noise ratio (SNR). We only need to plug in the trace and the algorithm does its work, yielding the intensity over time, the spectrum, and ultimately the electric field.

1.2.6 Second harmonic generation FROG in the mid-infrared spectral range

In 2010, P. K. Bates published the first full description of a SHG-FROG characterization device for mid-IR pulses [14]. By an interchange of crystals and detectors, the system is capable of measuring pulses with wavelength ranging from 800 nm to 5 µm and with temporal ranges up to 100 ps. This system was used with high spectral resolution to measure complex pulses of under 10 electric field cycles.

A benchmark of multiple crystals was made with the SNLO software. To support these large bandwidths, a thin crystal (200 µm) was used, with the trade-off of reduced conversion efficiency. It was then a matter of balancing the efficiency, the bandwidth, and of course, availability and price. Silver thiogallate ($AgGaS_2$) was found to be the most appropriate choice. Additionally, all the reflective surfaces of the remaining optics are gold-coated to preserve the broad bandwidth.

A test run in a 3200 nm centered wavelength pulse with energy of 1.2 µJ and spectrum covering 600 nm achieved a FROG error of 0.0025. The pulse had a duration of 9.0 cycles.

1.3 Structure of thesis

This Thesis is organized as follows.

- **Design and dimensioning of the FROG diagnostic setup**

We will first look into the requirements the setup has to fulfill in order to obtain an accurate measurement, namely the large bandwidth and dispersion. Dispersion is the phenomenon by which the phase velocity of a wave is dependent on its frequency and as such, carelessly treating the beam can affect the pulse temporal structure. Special attention will be given to the SHG crystal due to its key role in the setup.

We will then present a design of a SHG-FROG suitable to tackle the challenges of an ultrashort pulse in the mid-infrared by carefully choosing each component.

The ptychographic algorithm will be benchmarked by comparing it with other traditional FROG retrieval algorithms.

- **Alignment and operation of the FROG apparatus**

We will show the final FROG diagnostic, and how the data acquisition was controlled. A very useful characteristic of the 3 µm laser we intend to study is that it presents the Carrier Envelope Phase (CEP) stabilization. This ensures that all the pulses emitted by the laser are strictly the same in terms of the pulse phase-to-envelope offset. This is crucial for few-cycle optical pulse such as our own (four cycles of the electric field). Otherwise, we would have to develop a different mechanism to capture the data in a single-shot manner, that is, using a single pulse.

This experimental work involves acquiring several measurements with a very small distance between them (of the order of the µm). For that, a precision stepping motor will be used, not only to save time, but also to attain the precision we need. We will present the programming of the motor, and how it is articulated in parallel with the spectrometer so that a single spectrogram acquisition is fully automated.

- **Experimental results and discussion**

We will finally present the data retrieved and then analyse it. Two trial runs will be executed first using two 1 µm lasers whose pulses we already knew in order to verify that our device works properly. Finally, we will characterize the final 3 µm mid-infrared laser.

Chapter 2

Design and dimensioning of the FROG diagnostic

As with every experimental work, the calibration of the setup and the tools plays a central role in obtaining satisfactory results. For that, a quality design must be elaborated and each component carefully selected in order to accommodate the specifications of the phenomena we are studying.

In this chapter we will thoroughly look into what exactly are the challenges of the FROG in the mid-infrared and how we can overcome them. We will begin by introducing the reader to a generic FROG diagram. We will then present the design requirements of this work in particular. After setting forth our choice of components, we will look into detail on the choice of the SHG crystal. We will finally advance our final design. Following that, we will study the difference in performance of the ptychographic algorithm in comparison with a traditional one.

2.1 A FROG diagnostic setup

Before discussing any of this, we first need to know what a generic FROG diagnostic setup looks like. Figure 2.1 presents a diagram of one.

Following the beam trajectory, the first key component that it encounters is the beamsplitter. As explained earlier, the FROG technique needs to fuse a beam with another identical one to examine the combined characteristics. To carry through this fusion, as will be detailed later on, we opted for the Second Harmonic Generation (SHG) phenomenon. The easier way to obtain two identical beams is to split the original one and that's where the beamsplitter comes in.

We now have two beams following two different paths. One is simply redirected onward but the other is first delayed. The delay is, of course, carried out by making the route of the deviated beam vary from shorter to longer than that of the non-deviated beam. A combination of mirrors on a moving platform achieves that effect.

The two beams now need to converge into the crystal that produces the second harmonic. A converging lens or a concave mirror can be used for that. A second converging lens is used to collimate the diverging beam coming out of the crystal.

Finally, the spectrometer collects the data.

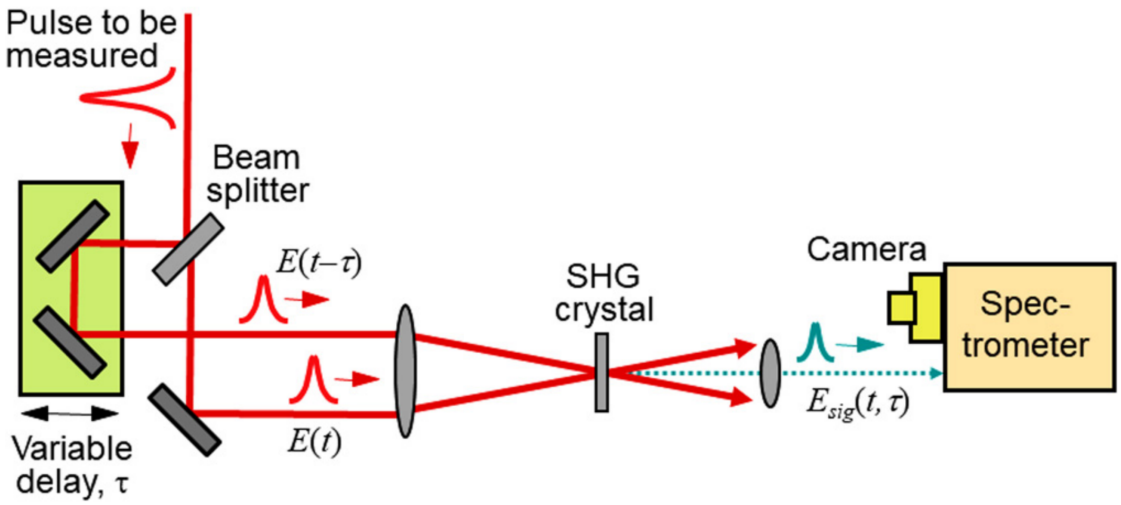

Figure 2.1: SHG-FROG diagnostic diagram [6, p. 14]. The initial beam is split in two in the beamsplitter. One of the beams is delayed, before recombining both in the SHG crystal. The detector captures the spectrum corresponding to that delay.

2.2 Design requirements

Taking into account the already discussed characteristics of the laser pulses, in particular their ultrashort duration, we know that dispersion is likely to be an issue. We will then preferably use components that are not transmitters, but rather reflective to prevent any material dispersion to take place.

Another issue is the pulse bandwidth. To anticipate the bandwidth our system should treat, we ran a simulation to estimate the minimum bandwidth of our 4 cycles laser corresponding to 40 fs at 3 µm assuming a Gaussian pulse using the Angewandte Physik & Elektronik (APE) tool [1]. The result was $\Delta\lambda$ = 330.98 nm, which is enormous. This means that we will have to use components suited to these characteristics to ensure that the spectrum is not cut anywhere.

In the case where there is no alternative to a transmitter component, then we will look to achieve a minimal width of said component in order to reduce its dispersion effect. Such is the case of, for one, the beamsplitter.

Now, for some more practical requirements. If we manually displaced the moving surface on top of which are positioned the mirrors introducing the delay, besides being less precise, each acquisition would drag on for a long time. This would not only be a waste of time, as well as increase the chances of incoherent readings as the changes in the conditions of the experiment are more likely to be noticeable. Indeed, changes in temperature or humidity, can affect the results, and the longer the experiment, the larger are the changes. Automating this process is then a prime concern.

Optical tables are often filled with multiple setups of other research projects. Another requirement is for the device to be compact in order to fit easily in the table and not disrupt any other experiment or device.

2.3 Optical components

As with every optics practical work, we will need mirrors to direct the beams as we want them, as well as irises for their alignment. Considering what we have discussed in section 2.2, we should look into

[1] Calculator - APE. URL: https://www.ape-berlin.de/en/calculator/ (visited on 01/09/2021).

the coating options. Protected silver mirrors were elected due to their high reflectance properties in the mid-infrared. In this wavelength range, these mirrors have an average reflection above 97%. While protected gold mirrors outperform these ones by 1%, we considered that this marginal difference did not justify a difference of 34% in the price [2].

As commented, we would prefer reflecting components instead of transmitting ones, and so, we opted for a parabolic mirror to focus the two beams in the crystal. This mirror is also coated with silver.

For the beamsplitter, we opted for a zinc selenide (ZnSe) due to its suitable transmission and reflection properties in the mid-infrared. Figure 2.2 shows the transmission curve. We see that at 3 µm we have around 55% reflection and 45 % transmission, which is rather standard for a beamsplitter, and so, it will perform as expected. In order to minimize dispersion, the beamsplitter is only 2 mm thick.

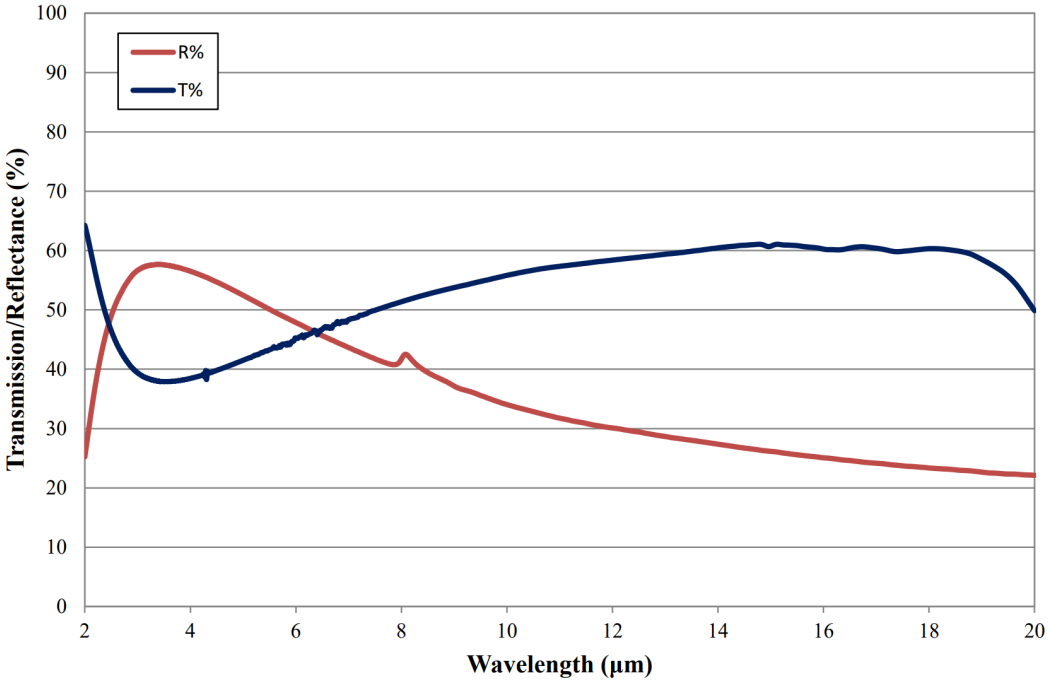

Figure 2.2: Zinc Selenide IR plate beamsplitter coating Performance

For the collimating lens we chose a CaF_2 spherical one. Since after the nonlinear crystal we have the desired mixing signal, the pulse duration after this point is no longer important so dispersion is not a major concern.

To solve the moving surface automation issue, we chose to use a translation motor acting on a linear translation stage. This motor would then need to be programmed, in parallel with the spectrometer so that they can work in sync and the diagnostic be fully automated.

In the following section, we will discuss the choice of a component that plays a key part in the setup; the crystal where the beam replicas are mixed.

2.4 Second-harmonic generation crystal

When high intensity light, such as a laser, penetrates a non-linear medium, its local properties are modified. This in turn modifies the light that goes through it. In this way, a non-linear medium allows light to interact with light. This is of particular interest to this work because of the need to recombine the

[2]Metallic Mirrors — Protected Gold, Silver, Aluminium Mirrors — EKSMA Optics. URL: https://eksmaoptics.com/optical-components/metallic-mirrors/ (visited on 09/22/2021).

two beams that were previously separated. Of the known phenomena that allows two beams to interact we can make use of the second-harmonic generation process. Other processes include using the electronic Kerr effect [15], Polarization-Gate (PG-FROG), Self-Diffraction (SD-FROG), Transient Grating (TG-FROG) and Second-Harmonic-Generation (SHG-FROG). FROG that uses a third-order nonlinearity in the polarization-gate geometry has proved extremely successful, and the algorithm required for extraction of the intensity and the phase from the experimental data is quite robust. However, for pulse intensities less than around 1 MW, such as our 3 µm OPCPA, third-order nonlinearities generate insufficient signal strength [16], so this technique was not suitable for this work. But SHG-FROG is appropriate for few-cycle pulses [17] and is the most popular among these techniques because it introduces little material dispersion before the non-linear process occurs [18]. Moreover, SHG FROG achieves the best signal-to-noise ratios because it is the strongest (lowest order) non-linearity and its signal beam is of a different wavelength, so scattered light is easily filtered [6]. We thus opted for the SHG-FROG.

2.4.1 Crystal selection

A suitable crystal must then be selected. For that the software SNLO [19] was used. Among other features, it allows us to input the conditions in which our laser operates and simulate the phase matching properties of a given crystal. A key property is the conversion efficiency of the crystal to produce the second harmonic across the bandwidth. Should some wavelengths be more affected than others, the signal will be distorted and not offer a trustworthy representation of the second harmonic. Unfortunately, this is unavoidable; it is quite uncommon to have a crystal that has full efficiency across the spectrum for ultrashort pulses, where the bandwidth is large. This study is about finding a compromise between more losses in some portion, but full transmission overall.

We are looking for a crystal with a wide bandwidth and a large conversion efficiency. The conversion efficiency is given by d_{eff} in pm/V, and the crystal acceptance bandwidth is given in Ghz·cm. However, a more meaningful unit for this bandwidth is the nm to compare it with P. K. Bates' article [14] and the result found in the previous section. So, to convert it:

$$\Delta\lambda[\text{nm}] = \lambda[\text{nm}] \cdot \frac{\Delta\mu[\text{GHz}]}{\mu[\text{GHz}]} = \frac{\lambda^2[\text{nm}]^2 \cdot \Delta\mu[\text{GHz}]}{c[\text{nm} \cdot \text{GHz}]} = \frac{\lambda^2[\text{nm}]^2}{c[\text{nm} \cdot \text{GHz}]} \cdot \frac{\Delta\mu[\text{GHz} \cdot \text{cm}]}{d[\text{cm}]} \tag{2.1}$$

where λ is the wavelength, μ the frequency, d the thickness of the crystal, and c the speed of light. Notwithstanding this conversion is that we must assume a crystal thickness to proceed with the calculations. A good first approach is to use the same one used in P. K. Bates' work, $d = 200\ \mu$m.

There are several types of phase matching, depending on the orientation of the polarizations of the incoming beams. As no component in the FROG device rotates the polarization, we are only interested in same polarization phenomena. Both beams can be in the ordinary axis or both in the extraordinary axis, so type I, IV, V or VIII phase matching are applicable. We thus retrieved the following information from the crystals that fit the description and are transparent to the 3 µm pulse and its second harmonic. Table 2.1 ranks the crystals from broadest to thinest bandwidth. From P. K. Bates's work, we can eliminate the crystals with $d_{\text{eff}} \leq 1$ for having too low conversion efficiencies. We now look to those with the highest bandwidth and preferably higher conversion efficiency. Ranking them by bandwidth from highest to lowest, the top crystals are $LiGaSe_2$, $LiInS_2$, $AgGaGeS_4$, $LiGaS_2$, $LiIO_3$, $HgGa_2S_4$, and $AgGaS_2$. Of all of these, only the $AgGaS_2$ crystal is readily available, and while it is not the one with the largest bandwidth, it is the one used in the previously cited work, which gives us more confidence in its suitability. As such, we opted for this crystal, the silver thiogallate, to obtain the second harmonic.

Table 2.1: Characteristics of crystals transparent in the suitable spectrum range ranked from highest to lowest bandwidth [19]. θ is the phase-matching angle, $\Delta\theta$ is the angular acceptance, and $\Delta\lambda$ is the acceptance bandwidth.

Crystal	**Transparency Range (nm)**	θ **(deg)**	d_{eff} **(pm/V)**	$\Delta\theta$ **(mrad)**	$\Delta\lambda$ **(nm)**
$LiGaS_2$	320 - 11600	53.2	-4.47	354	4372
$LiInS_2$	400 - 12000	42.9	-4.71	348.5	2841
$AgGaGeS_4$	700 - 13000	56	4.18	301	2293
$LiGaSe_2$	370 - 13200	52.3	-7.50	289	2011
$LiIO_3$	300 - 6000	21.5	1.56	146.5	1790
$HgGa_2S_4$	500 - 13000	41.9	23.80	350.5	1705
$AgGaS_2$	500 - 13000	37.5	9.53	288.5	1652
$La_3Ga_5.5Nb_5O_{14}$	430 - 6800	60.7	0.65	635.5	1625
$La_3Ga_5.5Ta_{.5}O_{14}$	500 - 6000	70.1	0.26	974.5	1596
$LiInSe_2$	500 - 12000	42.7	-5.28	311	1412
$BaGa_2GeSe_6$	580 - 16000	31.4	24.50	224	1262
$AgGaGe_5Se_{12}$	600 - 16000	62	14.40	113.5	1015
$RBe_2BO_3F_2$	165 - 3500	33.8	3.04	233	1008
GaSe	650 - 18000	15	56.00	77	928
HgS	630 - 13500	20	51.50	99	925
$CsBe_2BO_3F_2$	150 - 3500	41.1	0.30	269	893
$KBe_2BO_3F_2$	147 - 3500	33.3	0.31	204.5	889
$Na_3La_9O_3(BO_3)_8$	200 - 3500	36.2	1.50	189	866
$LiGaTe_2$	500 - 15000	35.8	40.80	171.5	833
Ag_3AsS_3	600 - 13000	20.6	23.60	92	826
$K_2Al_2B_2O_7$	180 - 3600	43	0.25	234.5	746
$KNbO_3$	400 - 4500	37.9	5.66	121	700
$CdSiP_2$	660 - 6500	64.7	79.70	390	617
$LiNbO_3$	330 - 5500	56	-3.82	225	608
$Li_2B_4O_7$	160 - 3500	63.3	0.08	366	510
$YCa_4O(BO_3)_3$	220 - 3500	170.8	-0.38	751.5	452
Ag_3SbS_3	700 - 14000	42.8	14.30	104.5	323
Tl_3AsSe_3	1250 - 20000	47.3	41.10	77.5	200

2.4.2 Silver thiogallate - AGS

Among the characteristics of the crystal, the first that we had to check was the interaction type. It is a type I phase matching, so both incoming beams have ordinary polarization, as intended. This interaction type does not require us to rotate polarization before splitting the beams, which means one less component that could introduce dispersion.

The second criteria was the transmission. The software SNLO gives the transmission shown in Figure 2.3. As we can see, in our range of interaction (3000 nm), there is indeed a quite satisfactory transmission of around 0.7.

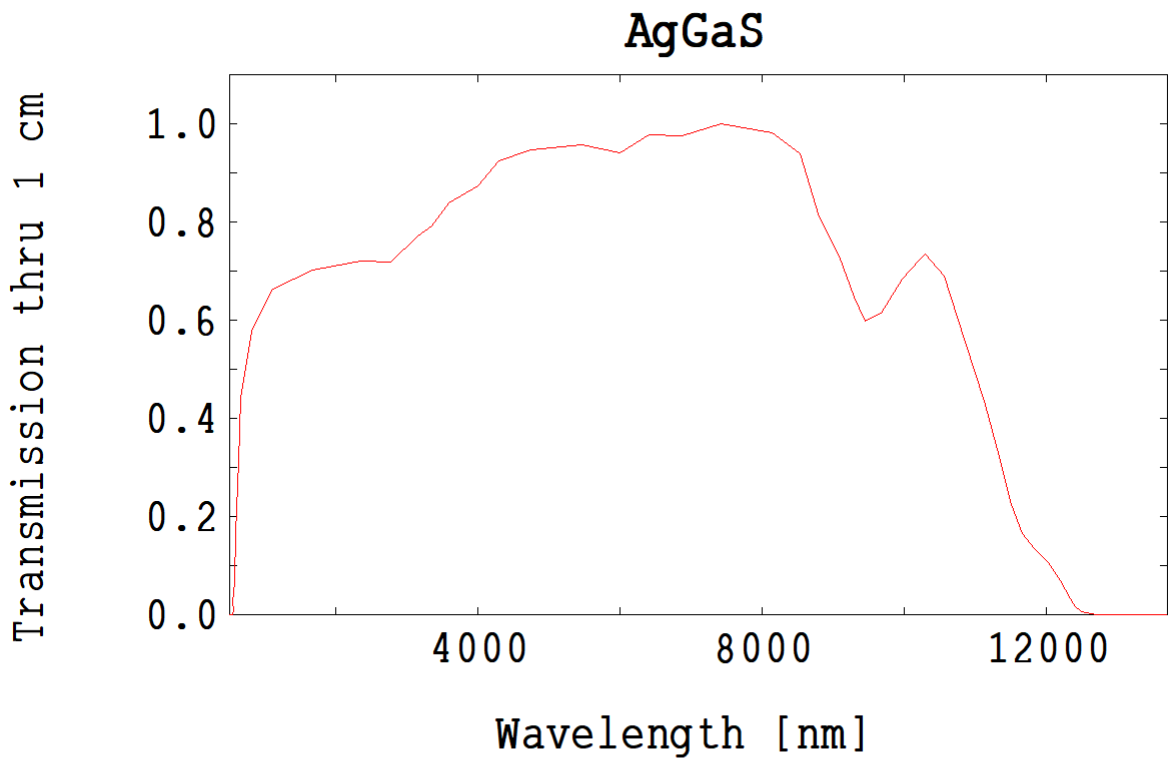

Figure 2.3: Silver thiogallate transmission [19]

Regarding the conversion efficiency, we know that the power conversion efficiency of the second harmonic generation is proportional to $d_{\text{eff}}{}^2$ [1]. While comparing with other options, we see that the top d_{eff} coefficients can reach values 10 times higher than for AGS. This means the power conversion efficiency with these crystals will be 100 times higher. However, we are already ensured by P. K. Bates' work that it is adapted to this application.

Finally, we still have the option to choose another thickness for the crystal, instead of the 200 µm. However, here comes into the equation the needs of the laboratory and other research, so it is not only the matter to find the best thickness for this specific application, but one that would work also for other ones. We needed the crystal to have the larger bandwidth possible. As shown in [1], the conversion efficiency η_{SHG} is proportional to the interaction length, in other words, the thickness of the crystal, squared. On the other hand, as shown in equation 2.1 the nonlinear-optical phase-matching bandwidth is inversely proportional to the crystal thickness. We have then to reach a compromise between conversion efficiency and bandwidth size.

Confident that the power of our beam ($\approx$ 4.5 W) could comfortably support a loss of factor of 4 (due to

the squared factor) in the efficiency to obtain a doubling of the bandwidth, we finally opted for a thickness of 100 µm. We thus have a bandwidth of 3250 nm, which is amply sufficient for our application.

2.5 Optical design

Given the requirements, we reach the design illustrated in Figure 2.4. Table 2.2 lists all components used in the diagnostic.

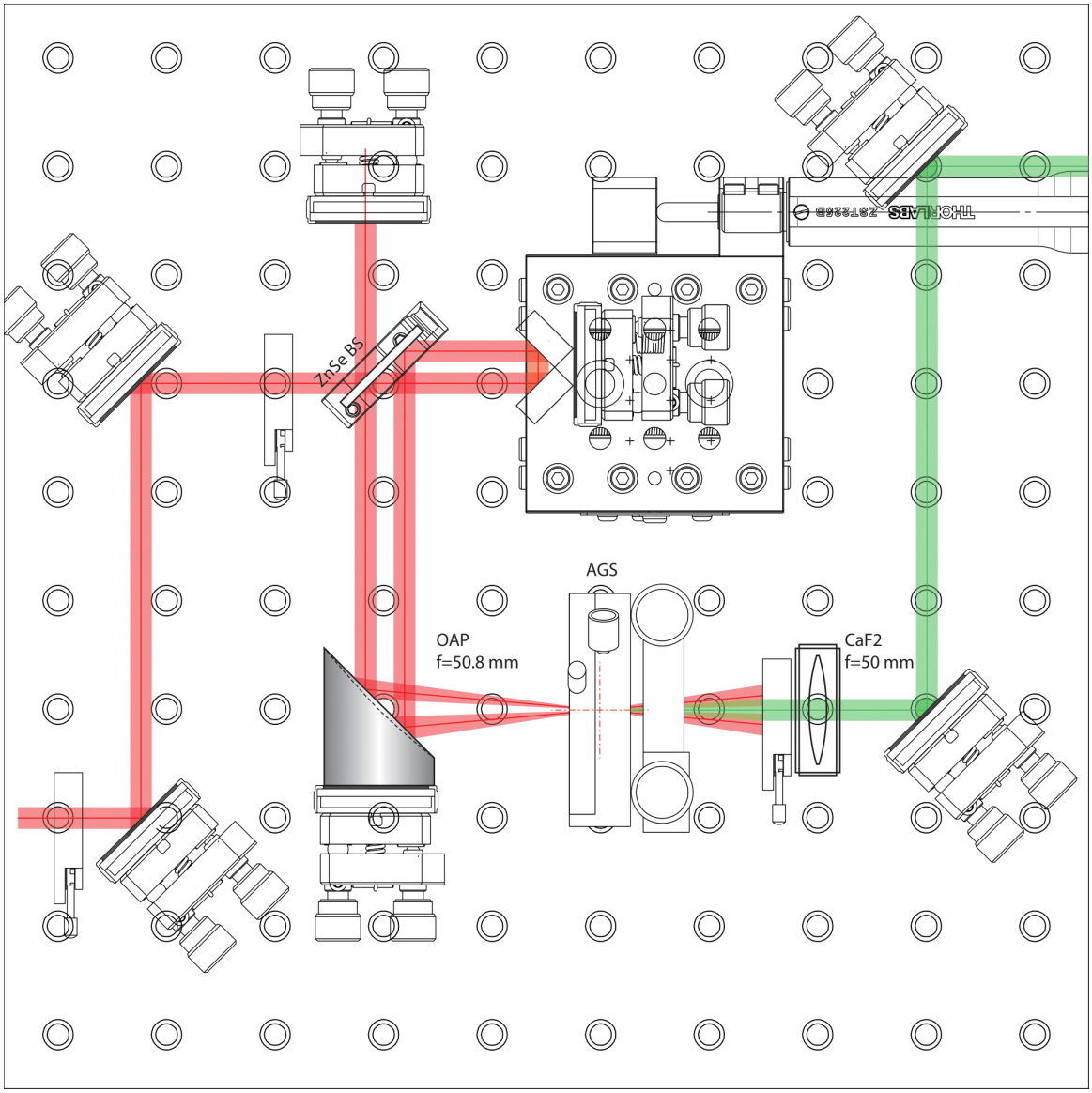

Figure 2.4: Design of our SHG-FROG. From the entry point on the left, the beam goes through an iris two mirrors, and another iris. The beamsplitter splits the beam. One part is reflected back in a mirror, the other in the retroreflector on top of the linear translation stage. Both beams move on to the concave mirror and to the crystal. A lens with an iris mounted on it collimates the beam. Two mirrors redirect the beam to the exit.

Instead of a combination of mirrors on top of a linear translation stage to produce the delay, as illustrated by the green block in figure 2.1, we opted for a retroreflector. This is simply a two-in-one version of what we intended to use. Notice that there are four more mirrors than strictly necessary in the entry and exit point. This is standard procedure in optics, in order to have control over how the beam

enters and exits the setup. Along with the two mirrors in the entry point come two irises. This eases the alignment operation when the setup is complete.

The beams need to arrive to the parabolic mirror not overlapped, so a shift is introduced in the retroreflector.

Table 2.2: List of components

Type	**Item**	**Brand**
Optomechanics	Breadboard	Thorlabs
Optomechanics	6X mirror supports Ø25	Thorlabs
Optomechanics	1X precision support Ø25 for parabolic mirror	Thorlabs
Optomechanics	3X irises	Thorlabs
Optomechanics	Beamsplitter support	Thorlabs
Optomechanics	Crystal support	Eksma
Optomechanics	Lens support Ø25	Thorlabs
Optomechanics	Linear translation stage	Thorlabs
Optomechanics	Posts, post supports and bases for every element	Thorlabs / Radiant
Optomechanics	Linear actuator 25 mm	Thorlabs
Electronics	Translation motor 25 mm	Thorlabs
Optics	5X protected silver mirrors	Eksma
Optics	Retroreflector mirror	-
Optics	ZnSe beamsplitter	Edmund Optics
Optics	Lens Ø25 mm f=50 mm CaF2	Eksma
Optics	Non-linear AGS crystal	Eksma
Optics	Silver parabolic mirror 25 mm f=50.2 mm	Edmund Optics
Software	Controler	Thorlabs

2.6 Retrieval algorithm: traditional vs. ptychographic

The final aspect to look into before proceeding is our recovery algorithm. We mentioned that we were going to use a ptychography-based algorithm. We also presented the developers' data (Figure 1.9) on how this algorithm fared against others. But how exactly does it compare with the one that we were going to use if we did not have the ptychographic one at our disposal. Indeed, this is not the first pulse characterization work performed at the Laboratory for Intense Lasers , so we still have some tools from the previous measurement. At that time, Femtosoft, a software published by Rick Trebino's commercial company "Swamp Optics", was used, however, it has since been discontinued. We still hold a copy of it, and so, that would serve as our benchmark.

To demonstrate its effectiveness, the ptychographic algorithm's code begins by taking a known pulse and producing its FROG trace, on top of which is then added white Gaussian noise in order to simulate measurement conditions. The code comes with a pulse bank of 100 pulses to choose from and experiment with. We chose the first pulse for this test, one of the simplest ones. It then recovers the pulse as described in section 1.2.5.

Figure 2.5 shows the original simulated noisy FROG trace and the retrieved one. Visually, we can hardly see any differences.

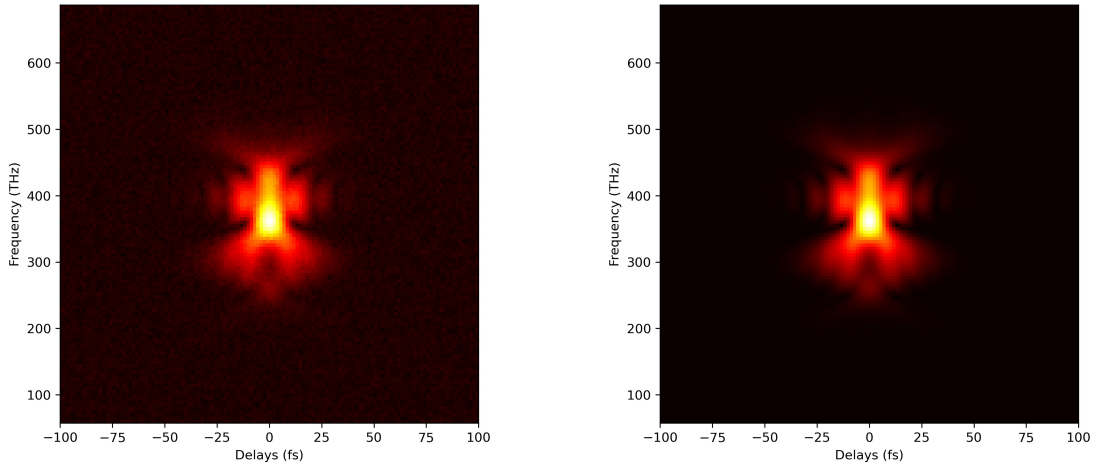

Figure 2.5: Visual comparison of the retrieved (right) and original (left) of the test pulse using the ptychographic algorithm

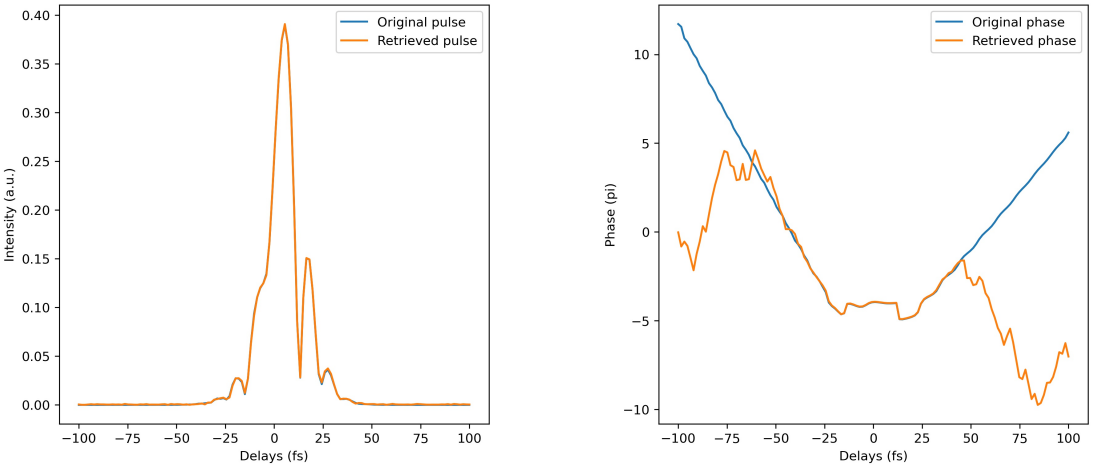

Figure 2.6: Comparison of the retrieved and original pulse (left) and phase (right) of the test pulse using the ptychographic algorithm

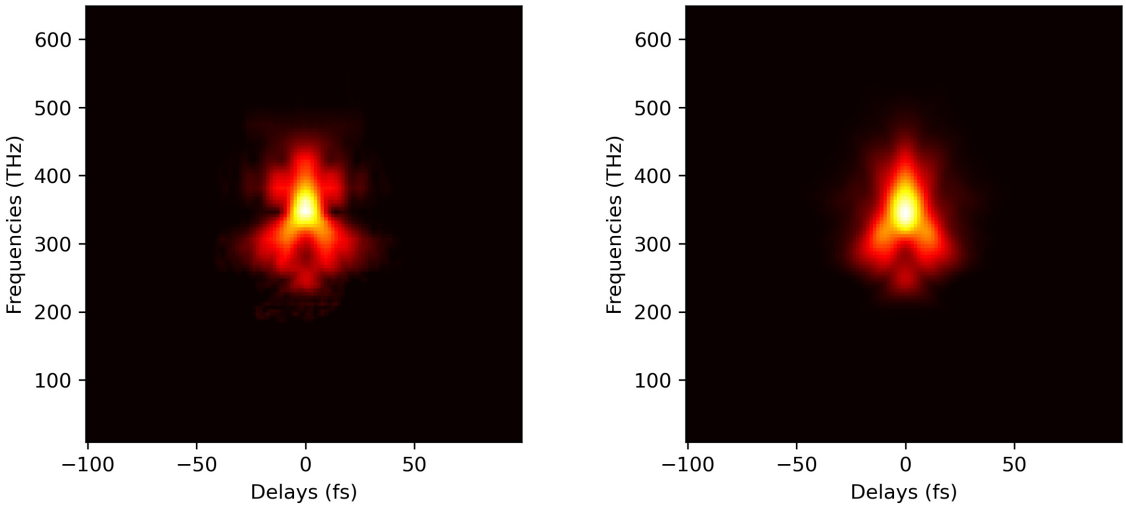

Figure 2.7: Visual comparison of the retrieved (right) and original (left) of a test pulse using Rick Trebino's software

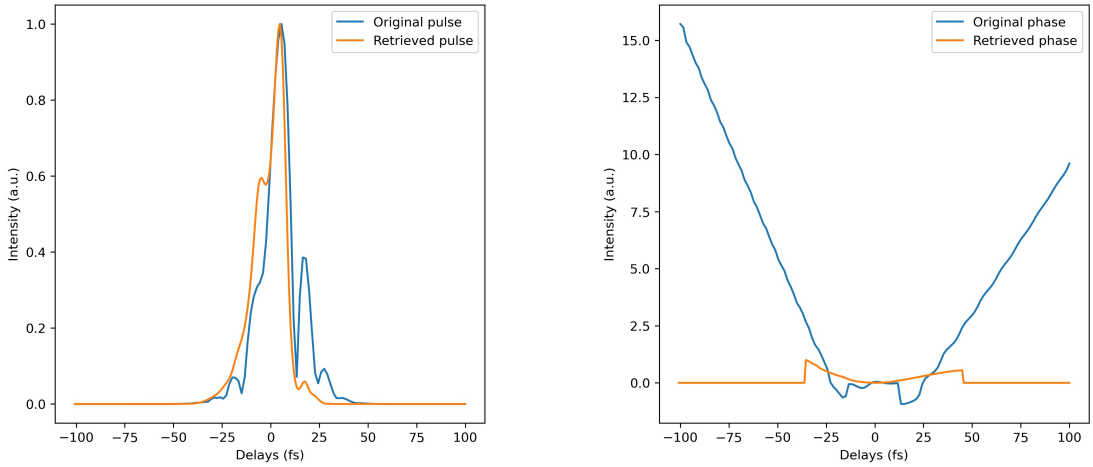

Figure 2.8: Comparison of the retrieved (right) and original pulse (left) and phase of the test pulse using Femtosoft

Next, comes the comparison of the retrieved pulse. We, of course, knew the original one, so we were able to compare it exactly. Figure 2.6 shows the nearly perfect overlap of the retrieved pulse and the original.

Finally, the phase was compared in figure 2.6. The phase holds no physical significance where the intensity is zero, and so, in the range in which there is intensity ([-30 fs, 30 fs]) there is again a nearly perfect concordance.

The quality of these results is in line with all the other pulses found in the pulse bank. The error reported in the recovery is of 0.009, which is more than satisfactory.

We then analysed the same pulse through Femtosoft. In order to do that, we first had to convert the spectrogram from a frequency vs time image, into a wavelength vs time image, as that is what the program received as an input. However, the conversion is not linear, but inverse, so we had to interpolate to ensure that we had an even spacing between pixels, and not a stretched spectrum.

From the input FROG trace, this tool applies multiple FROG retrieval algorithms, such as projections or projections-overstep, switching between methods when no improvement is seen after a number of iterations of that one given method. It keeps in store the iteration with the lowest error until a new, better one is found. The program can go looking for better solutions indefinitely. At some point, no better estimates can really be expected after all the methods have been tried a large number of times, each of them for a large number of iterations. When we conclude that no better estimate is likely to be found, we can terminate the process, and the software presents us with multiple characteristics of the retrieved pulse.

Figure 2.7 shows the visual comparison. A first step after introducing the data is to cleanup the noise a bit before running the algorithm, that is why the original trace is cleaner than with the ptychografic. But both retrievals where run with the same amount of noise initially, only, the ptychographic does this automatically. We can see that the algorithm misses some nuances. Although the least relevant, we see disparities in the outer region. We say they are less important because that region has a lesser weight in the calculation of the error than the central region, due to its intensity being lower. But looking at the central region, other aspects are evidently off, notably in the redder region, which instead of retrieving a star-like spot, it is more of an arrow head. This, being the region with the highest intensity, will have a larger impact on the error.

Regarding the pulse recovery (Figure 2.8), the differences really show. Although the general aspect (general width and center peak) are maintained, not much can be said about the shape. We still have the bump on the left-hand side, but the second peak on the right is missing all-together.

Figure 2.8 also shows the phase. Some kind of plateau seems to have been recovered, but aside from that, it seems to be rather off.

The algorithm reports an error of 0.017, which is about double that of the ptychographic, despite the large disparities observed. But one thing that we can say about this algorithm, is that it is very consistent with its results, meaning that different runs of the algorithm will retrieve very similar pulses. So the result will not depend on the way we cut data or cleanup the noise manually as it requires us to do.

In closing, we can say that the ptychographic algorithm does provide much more confidence as to its precision, and this benchmark attests to its robustness to noise in comparison with others. Nevertheless, the pulses that we will be characterizing are less nuanced than this test pulse. They will be more of a traditional ”spot” type of pulse, so we expect Rick Trebino's software to perform better and thus have more confidence in its results.

To make sure of that we created a Gaussian pulse with only a real part and ran it through both algorithms again. In the ptychografic algorithm, everything went smoothly as expected, although it maintained an error of 0.01. But Femtosoft did indeed produce satisfactory results with an error of 0.005 as shown in Figure 2.9. However, the comparison of the phase shows the algorithm retrieved a chirp in the phase, which we did not introduce when we generated the pulse. We can then rely on this software for the retrieval of the temporal intensity of simple pulses, but have to be doubtful as to its retrieved phase.

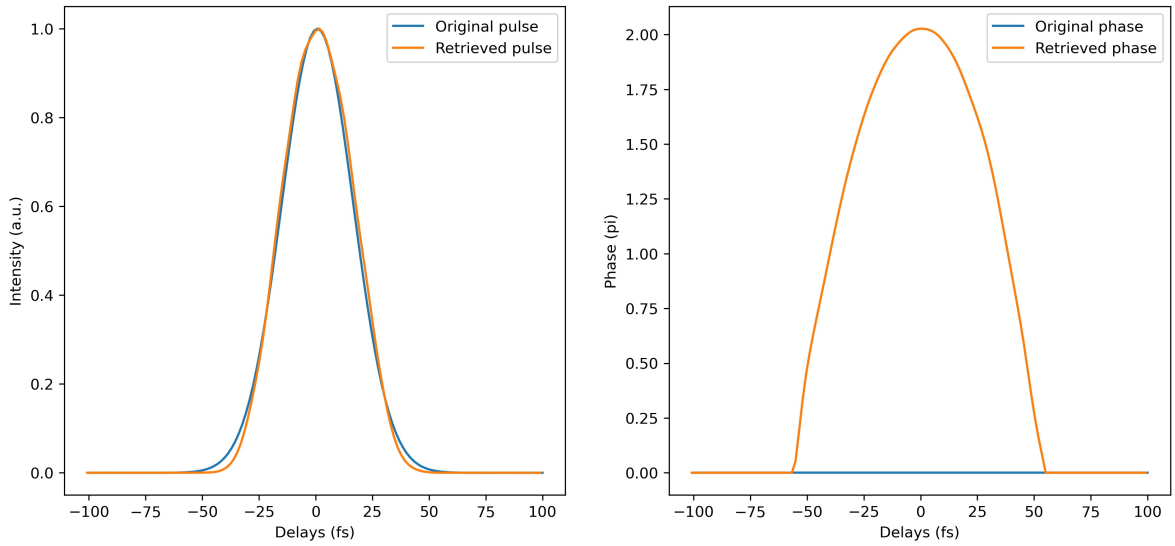

Figure 2.9: Comparison of the retrieved and original pulse (left) and phase (right) of a Gaussian pulse using Femtosoft

We have thus presented in this chapter the design of the diagnostic, with the highlight being on the choice of the 100 µm AGS crystal. We have also showed how the ptychographic algorithm outperforms our older alternative, Femtosoft, but that the later is still trustworthy for the temporal intensity of simple pulses.

Chapter 3

Alignment and operation of the FROG apparatus

Having developed the design of the FROG, we are now able to describe how the setup of the apparatus took place.

There were three main elements that had to be put together. The FROG diagnostic itself, the motor programming and the spectrum acquisition. We first showcase the real mounted diagnostic. We then show how the data acquisition was automated, and how it was controlled with the measurement interface.

3.1 FROG diagnostic alignment

In the first stage of the alignment, instead of using our 3 µm invisible and dangerous laser, we used a visible, weaker one to simplify the task. This laser operated at around 500 nm. It was mounted at the height of 12.5 cm, the height of the 3 µm laser so that when it came to transfer the breadboard, everything was already at the appropriate height. Of course, this does not restrict our diagnostics' use to lasers mounted at that height, it only avoids the trouble of correcting the entry height for this case.

One might notice that the real diagnostic shown in figure 3.1 differs slightly from the design (Figure 2.4). The principal differences are the distances and the presence of a second linear translation stage on which the crystal is mounted. The distances are altered because the design does not take into account the bases and the clamps, which forced us to adapt parts of the setup. The translation stage was added to facilitate the alignment. The distance from collimating lens and the crystal was to remain fixed but we would still probably need to adjust the distance of the block to the parabolic mirror, so we opted to position the pinhole and the collimating lens on top of a manual translation stage.

Most components did not need to have their height adjusted during the work, they were all mounted on 1" posts. These types of posts are preferred because they provide more stability, and are less expensive than ½" inch posts on post holders. The parabolic mirror, the retroreflector, the crystal support and the lens were mounted on ½" inch posts, so that, if another laser was to be characterized the substitution of the key components would not entail a full realignment of the apparatus.

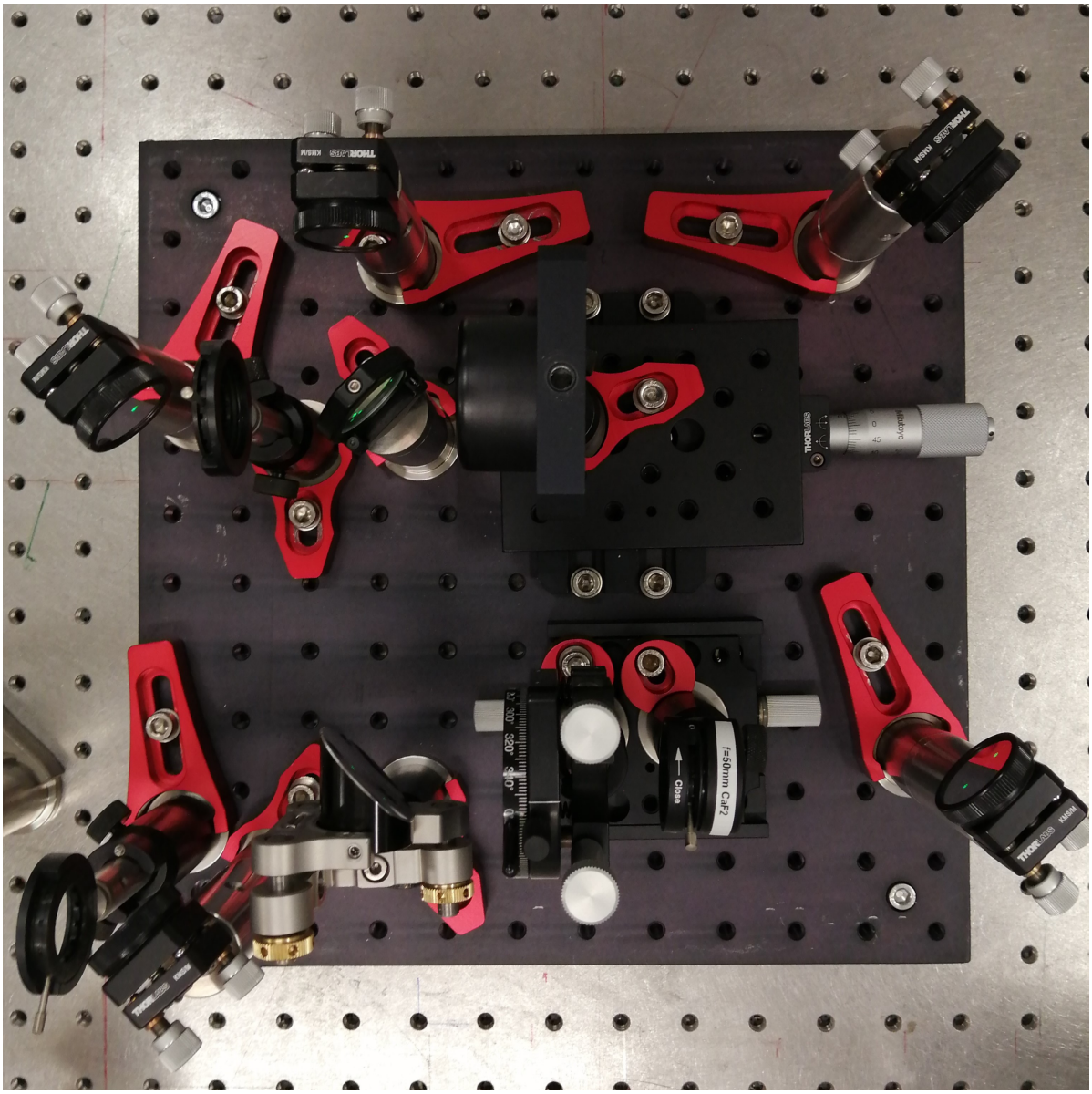

Figure 3.1: FROG diagnostic photograph. The beam enters from the lower left and exits from the upper right side. On the upper side are, from left to right, a mirror, an iris, another mirror and the beamsplitter, the retroreflector on top of a linear translation stage, and another mirror. On the bottom, an iris, a mirror, the parabolic mirror, the crystal support, a converging lens, and a mirror.

3.2 Step motor configuration

The FROG trace is essentially the spectrum of the SHG beam for multiple even delays of the deviated beam. As ultrashort pulses are in the order of the 10^{-13} s, we need even shorter delay intervals than that, something around 10^{-15} s to be able to obtain up to 100 measurements. This is achieved with a displaceable retroreflector mirror, so each movement will actually add the double of the length of the displacement to the beam route. The order of magnitude of the distance that introduces the time delay that we are looking for is $\delta d = 2 \cdot \delta t \cdot c = 2 \cdot 10^{-15} \cdot 3 \cdot 10^{8} \approx 10^{-6}$ m, where δt is the delay interval we are aiming at, and c is the speed of light. The space intervals needed are then in the order of the µm.

Even disregarding time effectiveness, such precision can hardly be obtained consistently using a manual translation stage. That is why an automated stepper motor is used, allowing also for rapid acquisitions. The one we used was the Kinesis KST101 Stepper Motor Controller from Thorlabs.

We now had to program the motor in order to operate it. For that, we used the software LabVIEW, a systems engineering software for applications that require test, measurement, and control with rapid access to hardware and data insights [1].

What we essentially wanted to obtain, is a control frame where we would input our time interval and the delay interval and have the motor go through that range. So first, we had to translate time into space. Figure 3.2 shows the calculation. ”t max (ps)” and ”t min (ps)” are the upper and lower limit of the interval, and ”delta t (ps)” the delay interval. Another input is the ”offset (mm)”, allowing to define a default position of the motor.

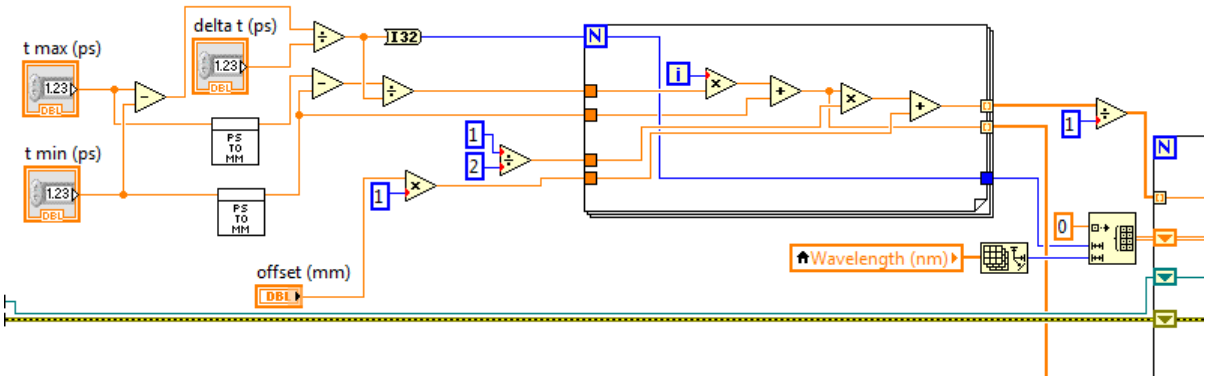

Figure 3.2: LabVIEW motor conversions block

After running through all the calculations, the position of the motor in mm was calculated for one particular iteration and passed through to the motor movement execution section of the code (Figure 3.3). The number of intervals (as well as the number of wavelength points calculated elsewhere) is printed in a file. Of particular interest, is the factor of 2 introduced in order to account for the fact that each physical displacement of the motor actually introduces the double of the distance of said displacement due to the return path of the beam.

The movement execution section (Figure 3.3) is here shown in its different stages. Essentially, after initialising the motor, the position is entered in the motor ”SetAbsMovePos” function, and then in the ”MoveAbsolute” function as we see in the image. Although not shown in the image we also implemented a function that re-positions the motor at the center of the interval when the acquisition is over, allowing to be at the position where the two peaks overlap perfectly. In the end the motor is shut down.

[1] What is LabVIEW? - NI. URL: https://www.ni.com/pt-pt/shop/labview.html (visited on 09/06/2021).

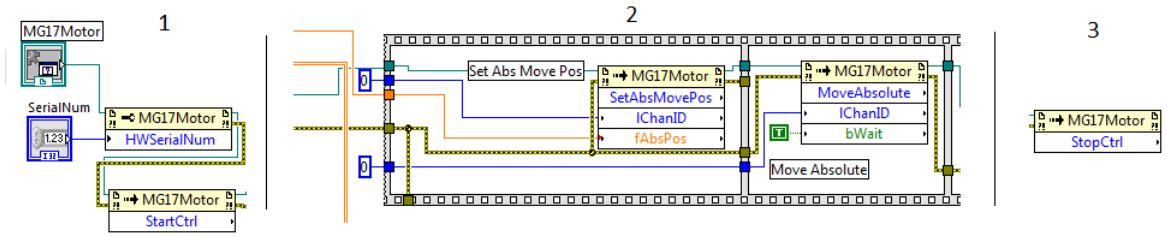

Figure 3.3: LabVIEW motor operation. (1) Motor initialisation. (2) Motor movement execution. (3) Motor shut down

3.3 Measurement interface

Now that we were able to obtain the delays, we only needed to obtain the spectrum for each of them. Again, instead of manually obtaining them, the process was automated using LabVIEW. This allowed to articulate the spectrometer with the motor, so that after entering the initial parameters, the program ran the acquisition in one go, retrieving the spectrum for each delay and printing the final result in a data file, ready to be analysed. In addition to that, our LabVIEW interface presented a series of widgets that allowed to easily control the parameters and see the results. Figure 3.4 shows the front panel of the program. There is a widget for the controlling of the motor (MG17Motor), another for the live spectrum (Spectral Waveform), and a final one for the final FROG trace (Intensity Graph). Aside from the time inputs already described in section 3.2 and the ”OK button” to start the measurements, we have two buttons of particular interest that allow to cancel the background noise; the ”Get Background” and ”Background Subtraction”. Finally we could alter the integration time of the spectrometer should the number of detections be too high or too low. The ”Save?” button allowed, of course, to save the file.

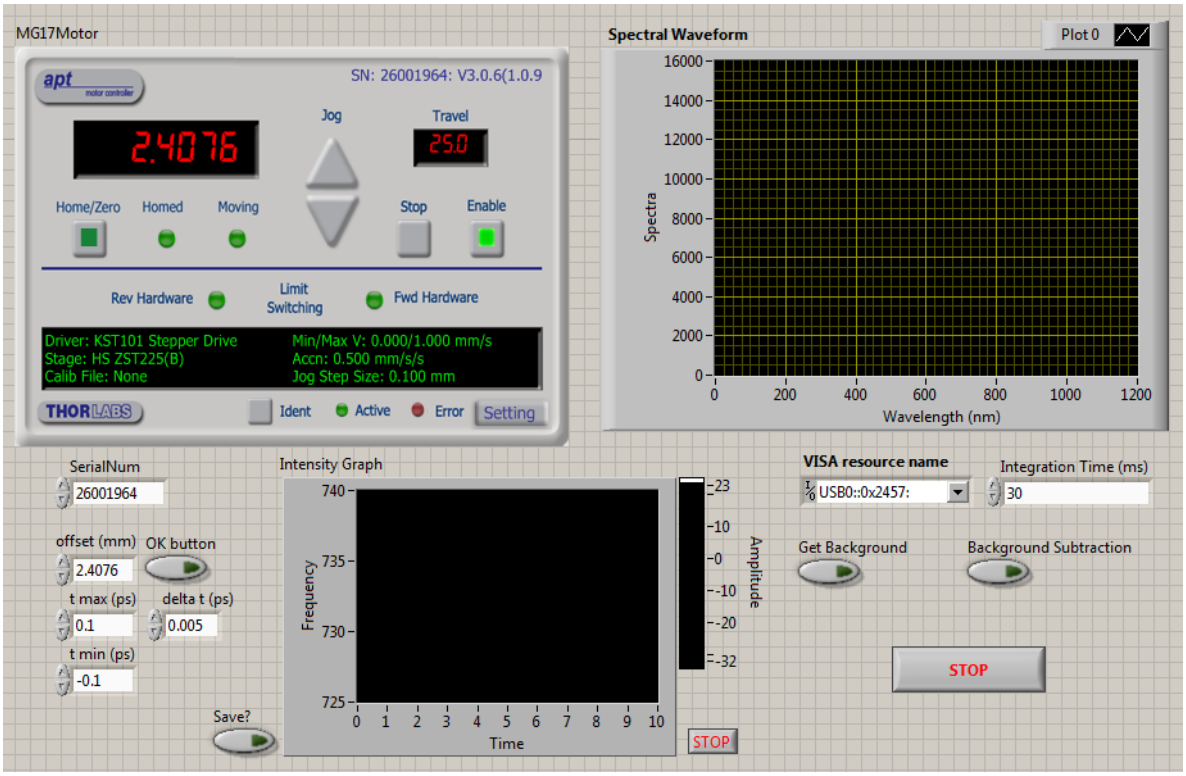

Figure 3.4: LabVIEW FROG front panel

Not everything goes as planned, and in our available time frame, we had not the opportunity to integrate the 3 µm spectrometer into our LabView program. So, instead of actually retrieving a FROG trace, we would now obtain the autocorrelation since we had a suitable photodiode, and knew how to use it. Although less precisely, we would still accomplish what we set out to do; to characterize an ultrashort mid-infrared pulse.

For that purpose, we devised a similar LabVIEW program. Figure 3.5 shows the front panel. Instead of the live spectrum, it now retrieves the live intensity in ”Waveform Graph 2”, and shows the final autocorrelation in ”Waveform Graph”.

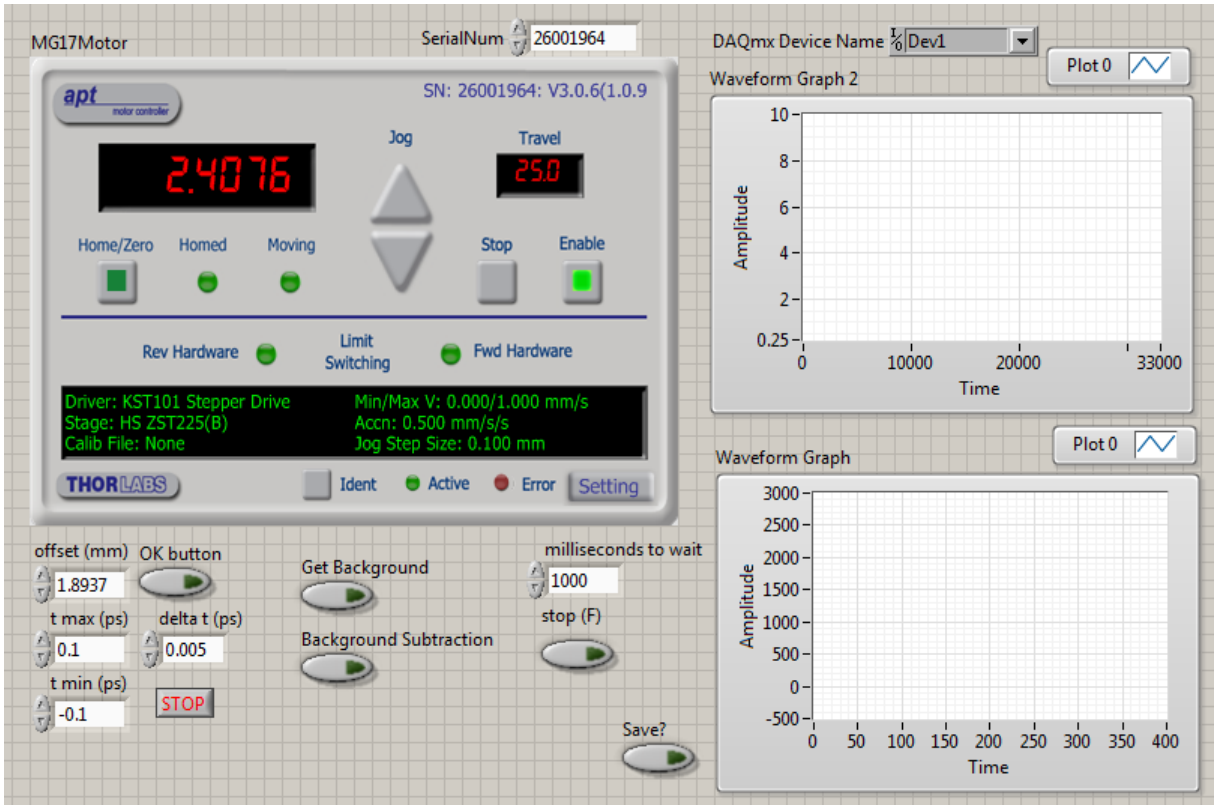

Figure 3.5: LabVIEW autocorrelation front panel

Appendix A shows the full block diagrams used in the work.

To sum up, we presented in this chapter the final setup and control interface of the data acquisition. We devised a way of obtaining a spectrogram, but also one that only captures the autocorrelation.

Chapter 4

Experimental results and discussion

All the preparations having been completed, We are now able to acquire data. In this chapter, we present the data retrieved and then analyse it. Two trial runs were executed first using two 1 µm lasers whose pulses we already knew. For both of these, we obtained and analysed the autocorrelation and then applied both FROG algorithms. Finally, we obtained the autocorrelation of the 3 µm laser.

4.1 Coherent Mira Ti:sapphire oscillator

The first laser we characterized is a coherent Mira Ti:sapphire oscillator, whose specifications are presented in Table 4.1.

Table 4.1: Coherent Mira Ti:sapphire oscillator laser parameters

Repetition rate	76.6 MHz
Pulse energy	$\approx$ nJ
Wavelength	1032 nm
Pulse length	$\approx$ 100 fs

At 1 µm, we are in the infrared region. The length of the beams route after their separation in the beamsplitter must be equal for both of them, and so the correct retroreflector position had to be found. This lasers' pulse length is of around 100 fs, so we would only see the second harmonic in an interval of $d \approx c \cdot t/2 \approx 15$ µm.

We scanned the delay stage in steps of 2 fs, over a range of 900 fs, corresponding to 450 points of delay with a step size of 0.3 µm. The spectrometer used was an Ocean Optics USB4000 Fiber Optic Spectrometer with an optical resolution of around 0.45 nm.

4.1.1 Autocorrelation

We obtained the autocorrelation by integrating the FROG trace in frequency. As commented in section 1.2.3, we have to make a guess regarding the pulse shape in order to estimate its width. Given the simple spot-like spectrogram retrieved (Figure 4.3) we assumed a Gaussian shape (a sech^2 could also have been appropriate), and applied its form factor to yield the approximated pulse width. Figure 4.1 shows the autocorrelation and the Gaussian function that best fits the data. The FWHM of the curve is of 248 fs, and thus, the pulse width is of around 248/1.414 = 174 fs. It fits in the order of magnitude we anticipated.

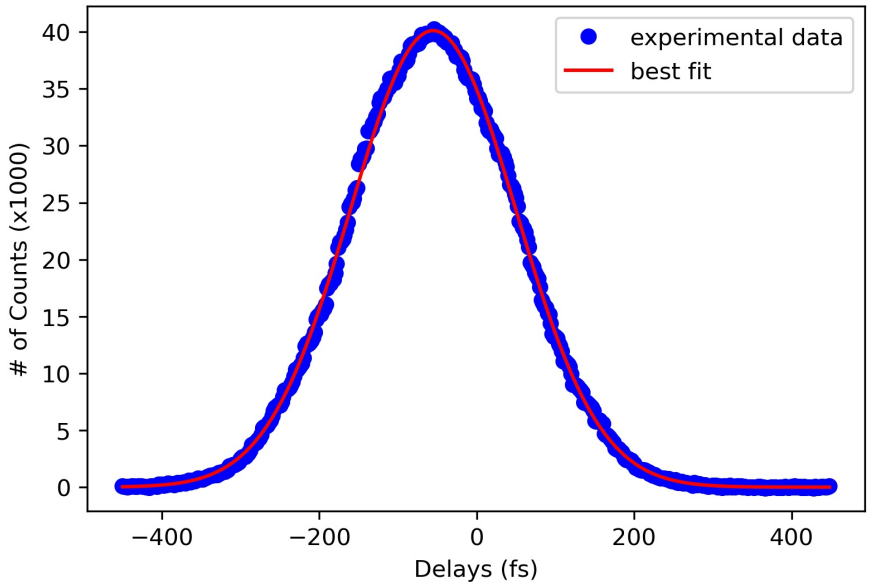

Figure 4.1: Gaussian fit of the oscillator autocorrelation data.

However, to check if this pulse width was physically possible we proceeded with a simple test. Equation 4.1 gives a relation between the wavelength peak λ, the bandwidth $\Delta\lambda$ and the pulse width $\Delta\tau$, and a quantity called the time bandwidth product, TBWP.

$$\Delta\tau \cdot \Delta\lambda \cdot \frac{c}{\lambda^2} = TBWP \tag{4.1}$$

For each pulse shape, there is a minimum TBWP possible. If our pulse width that we found previously resulted shorter than the minimum pulse width calculated with equation 4.1 by plugging in the minimum TBWP possible, then our measurement had to be incorrect. Assuming a Gaussian pulse, the minimum TBWP is 0.44, and the calculation reports a minimum pulse width of 128 fs which is indeed largely inferior to the 174 fs measured. This is a reassurance that the pulse is indeed possible.

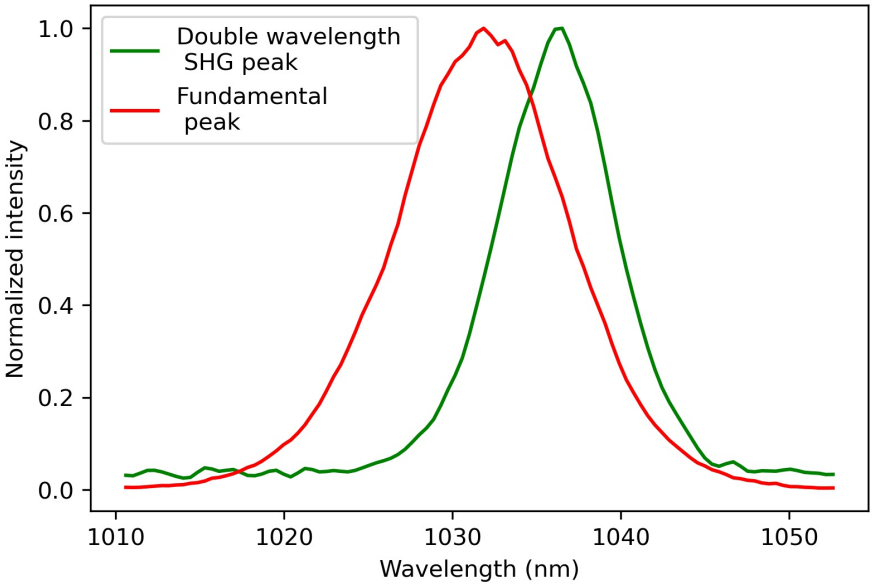

Figure 4.2: Plot of the oscillator spectrum of the fundamental pulse and of the second harmonic with its wavelength axis doubled.

We also ran a test to verify that the result was credible. It consisted in doubling the wavelength of each point of the spectrum of the second harmonic and compare it with the spectrum of the fundamental peak of the beam (the one coming directly from the laser). Again, the spectrum was obtained by integrating the FROG traces, but in this instance, in time. Figure 4.2 shows both spectra.

This test would serve two purposes. The first, to ensure that it was indeed the second harmonic that we were obtaining. The second, to check if there were any cuts in frequency. Theoretically, the two curves should overlap perfectly.

Fitting a Gaussian in both these curves we obtain the results presented in table 4.2.

Table 4.2: Comparison of the fundamental pulse peak parameters vs the doubled in wavelength second harmonic peak

	Fundamental	**Doubled SHG**
Peak center	1032 nm	1036 nm
FWHM	12.2 nm	9.4 nm

This remains a mostly qualitative test, and so the results were deemed satisfactory despite the differences. Indeed the spacing between wavelengths in the spectrometer is non uniform. The average difference between pixels in the spectrometer is of 0.449 nm. But the spectrometer is not completely linear; this difference varies from one end of the spectrum to the other. We are measuring a peak in the region we are certain the measurement is correct, the fundamental one, so we calibrated the data to match the 1032 nm. But the second harmonic is well outside that region, so, when doubling the indexes, the distortion and shift took place.

4.1.2 Femtosoft software

We then fully characterized the pulse using Swamp Optics's discontinued FROG algorithm application.

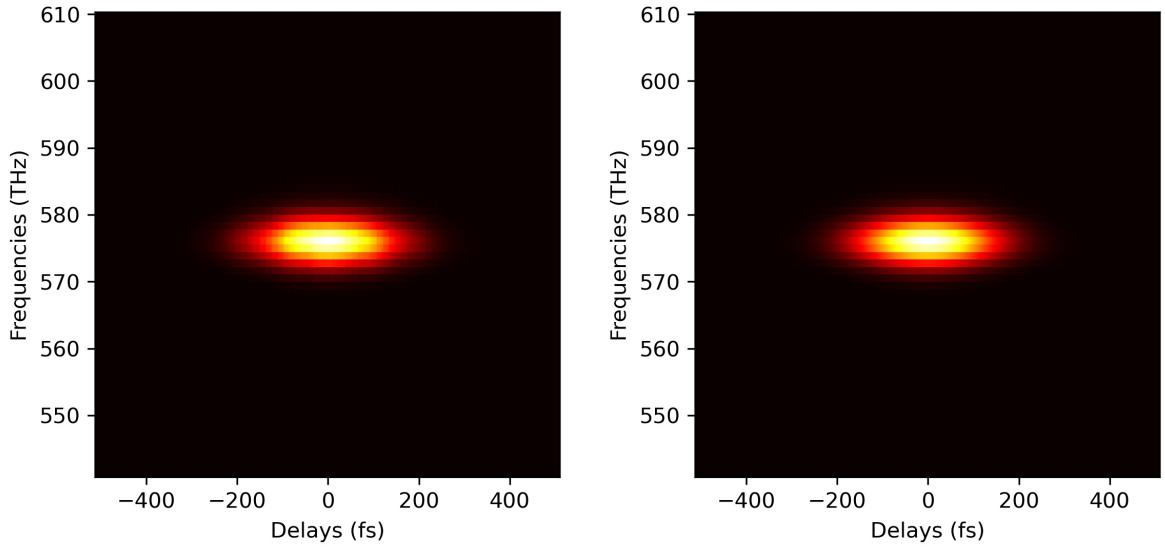

Figure 4.3: Visual comparison of the retrieved and original Ti:sapphire oscillator FROG trace using Femtosoft

Figure 4.3 shows the visual comparison between our input pulse (on the left) with the one retrieved by the software (on the right). Figure 4.4 shows the retrieved pulse and spectrum. Table 4.3 shows the retrieved parameters and the error in trace retrieval.

In comparison with the calculation of the pulse width using the autocorrelation, it is rather close. Indeed this pulse has a shape resembling that of a Gaussian, as attested by the similar TBWP, so our guess was pertinent.

Regarding the phase, we notice that the pulse has some chirp due to its parabolic phase, although, we cannot be sure of this due to the uncertainty created with the benchmark in section 2.6. A chirped signal has the frequency increasing or decreasing with time.

The error reported is very tiny. As commented in section 2.6, we need to be wary of this value. What it can be useful for is to compare with the error of the test characterization. The error then was of 0.017, which is 18 times larger than this one. As expected, this software effectively retrieves simpler pulses such as this one, so we can be more confident in its result than in our first benchmark pulse in section 2.6.

The pulse width is then of 188.2 fs, however, the error presented here does not correspond to the error of the pulse of this full technique, as it does not take into account the errors in retrieving the trace.

Table 4.3: Retrieved oscillator pulse parameters

Autocorrelation FWHM	250 fs
Temporal FWHM	188.2 fs
FWHM TBWP	0.609
Error	0.00095

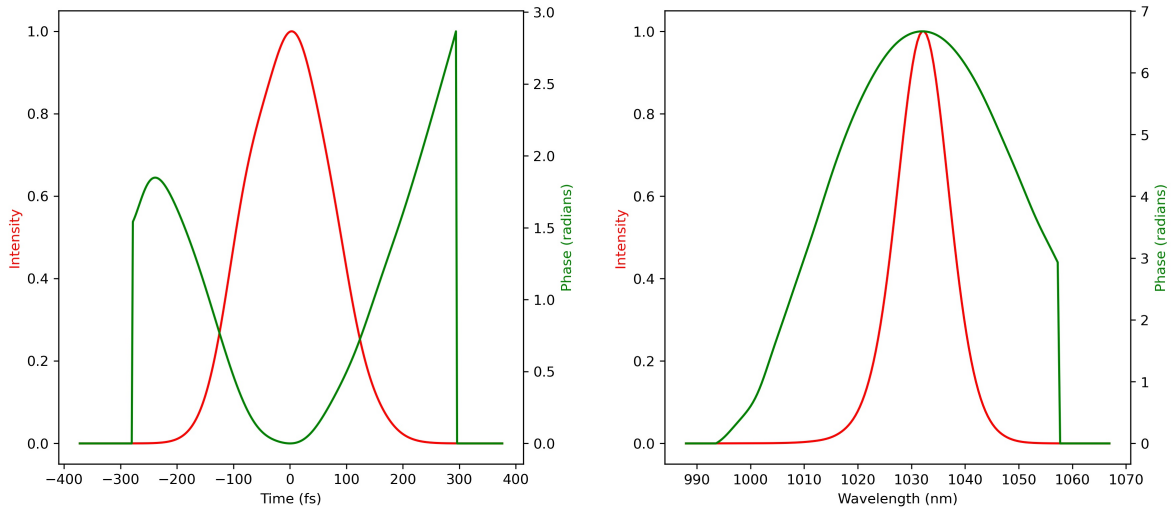

Figure 4.4: Retrieved pulse and phase (left), retrieved spectrum and spectral phase (right) using Femtosoft

4.1.3 Ptychographic algorithm

We finally ran the pulse through the ptychographic algorithm. Figure 4.5 shows the original and retrieved traces. We can see the retrieval was mostly successful.

The error reported is of 0.084. This large error can be explained by the squeezed format we had to input the data in. Indeed, the algorithm requires the data to be plugged in with the product $dt \cdot dF = 1/N$, where dt is the delay interval between pixels, dF the frequency difference between pixels, and N the grid size, i.e. number of pixels in an axis. We thus cannot stretch interpolating the data in wavelengths more to have more points. We would need a spectrometer with higher resolution for more precise results.

Fitting a Gaussian in the retrieved temporal pulse data (Figure 4.6) yields a pulse width of 201 fs. Of course, we are assuming that the pulse is Gaussian-like, but this assumption does seem accurate looking at the figure. This retrieval differs by 12.8 fs from Femtosoft. We have already talked about this application's efficacy in retrieving simple pulses, so, given the previous one presented an error 10 times smaller, we are more confident that 188.2 fs is the true value. Indeed, an 8.4% error in 201 fs represents the interval [184 ; 218] fs, which includes the 188.2 fs.

Regarding the phase, we can now see that this pulse has no chirp as opposes to the linear one in the previous section. Given the benchmark in section 2.6, we deem this one to be more trustworthy.

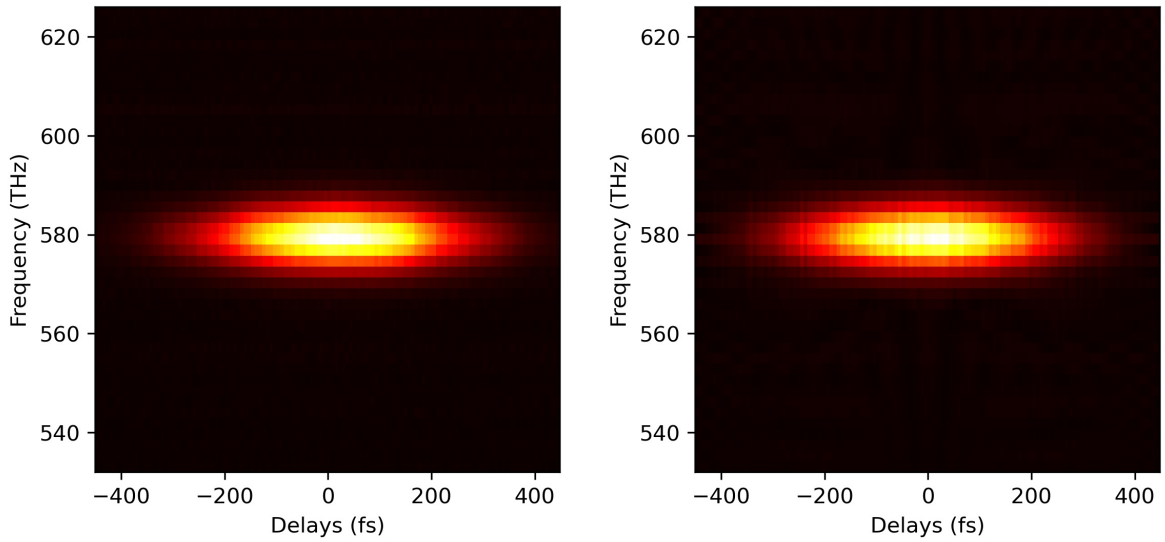

Figure 4.5: Original (left) and retrieved (right) oscillator FROG traces using the ptychographic algorithm

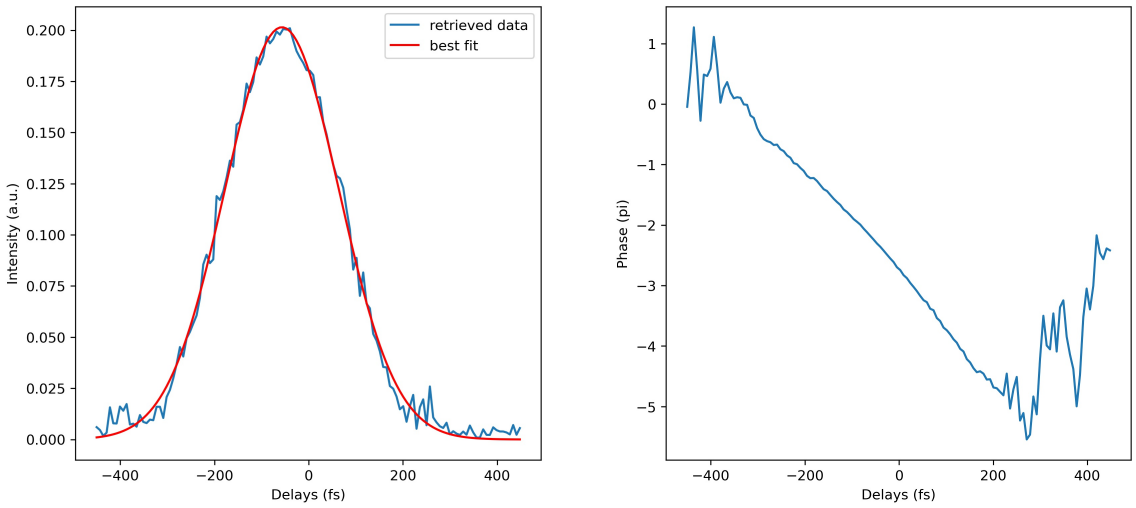

Figure 4.6: Retrieved oscillator pulse (left) and phase (right) using the ptychographic algorithm

4.2 Amphos Yb:YAG InnoSlab amplifier

We now characterize a second 1 µm laser. Table 4.4 shows its parameters.

We are again in infrared region. Given this laser's pulse width we have an interval of $d \approx c \cdot t/2 \approx 135$ µm for the retroreflector position.

Table 4.4: Amphos Yb:YAG InnoSlab amplifier laser parameters

Repetition rate	100 kHz
Pulse energy	1 mJ
Wavelength	1032 nm
Pulse length	$\approx$ 900 fs

We scanned the delay stage in steps of 20 fs, over a range of 8 ps, corresponding to 400 points of delay with a step size of 3 µm. The same spectrometer was used as previously.

4.2.1 Autocorrelation

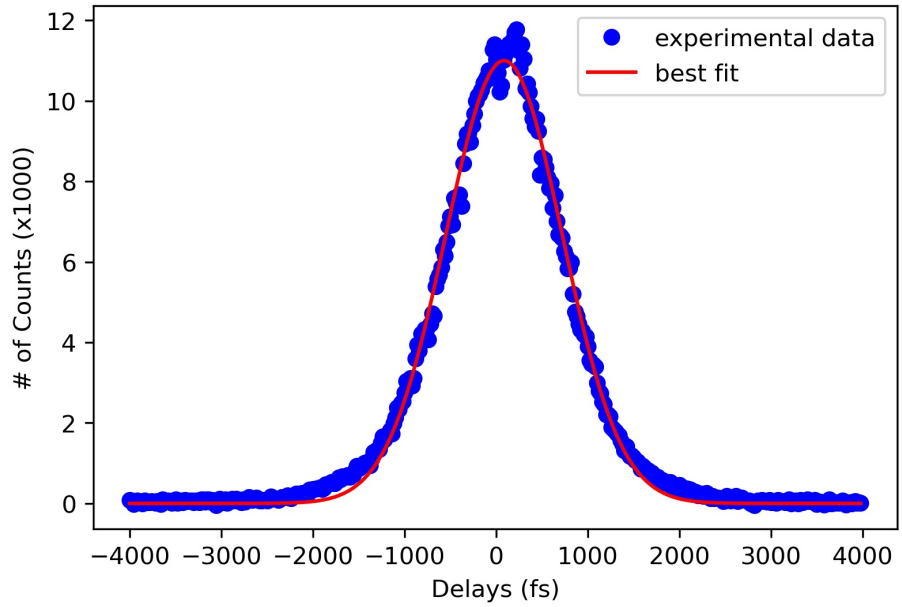

Figure 4.7: Gaussian fit of the amplifier autocorrelation

Starting again with the autocorrelation, figure 4.7 shows the experimental data and the best Gaussian fit. The FWHM of the function is of 1497.5 fs. Applying the form factor for a Gaussian pulse, we get 1498/1.414 = 1059 fs. This estimate fits in the order of magnitude that we expect the pulse width to be in.

Applying once again 4.1 with a Gaussian TBWP, we obtain a pulse width of 517.05 fs, which is shorter than the 1059 fs we just found, so a pulse with these characteristics is indeed possible.

Again, we followed with the study of the credibility of the results in terms of the validity of the second harmonic. Figure 4.8 shows the overlap between the fundamental peak and the second harmonic with its frequencies doubled. Table 4.5 shows the comparison of the FWHM and the peak center.

Table 4.5: Comparison of the fundamental pulse peak parameters vs the doubled in wavelength second harmonic peak

	Fundamental	**Doubled SHG**
Peak center	1032 nm	1034 nm
FWHM	3.03 nm	3.18 nm

Given the similarities in parameters found between the two curves, it is indeed the second harmonic that is being retrieved with no cuts. The differences in peak centers and width distortions from this laser

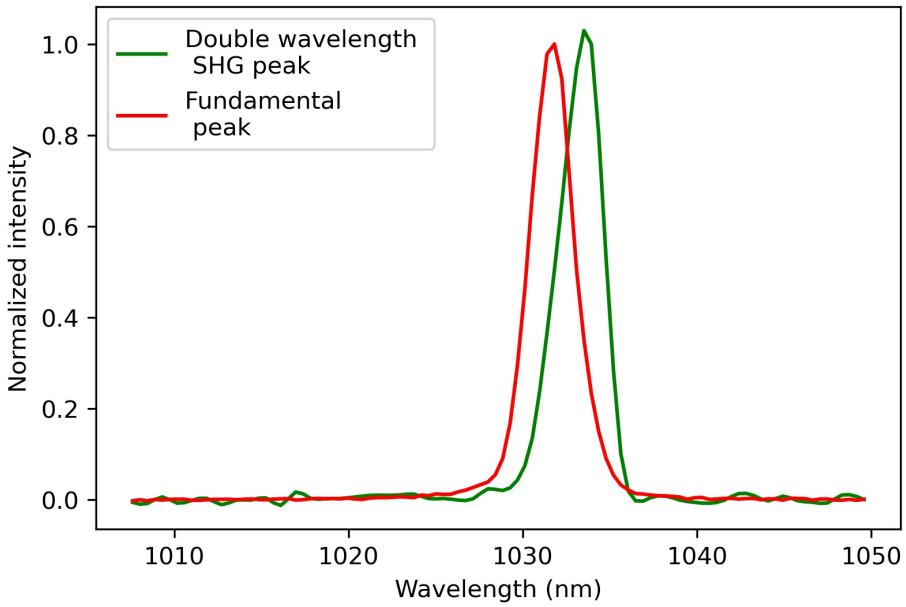

Figure 4.8: Plot of the amplifier spectrum of the fundamental pulse and of the second harmonic with its wavelength axis doubled.

to the other are certainly due to the great difference in bandwidths between both lasers.

4.2.2 Femtosoft software

Running through Femtosoft again, we find satisfactory results. Figure 4.10 shows the visual comparison of the original and retrieved FROG trace. As we can see, the original FROG trace is slightly less "Gaussian" than the previous one, with a slight tail on the upper part of the picture. The bulk of the pulse represented with the hotter colors (red/yellow) is very similar to the original one. Table 4.6 shows the error is still tiny at 0.3%.

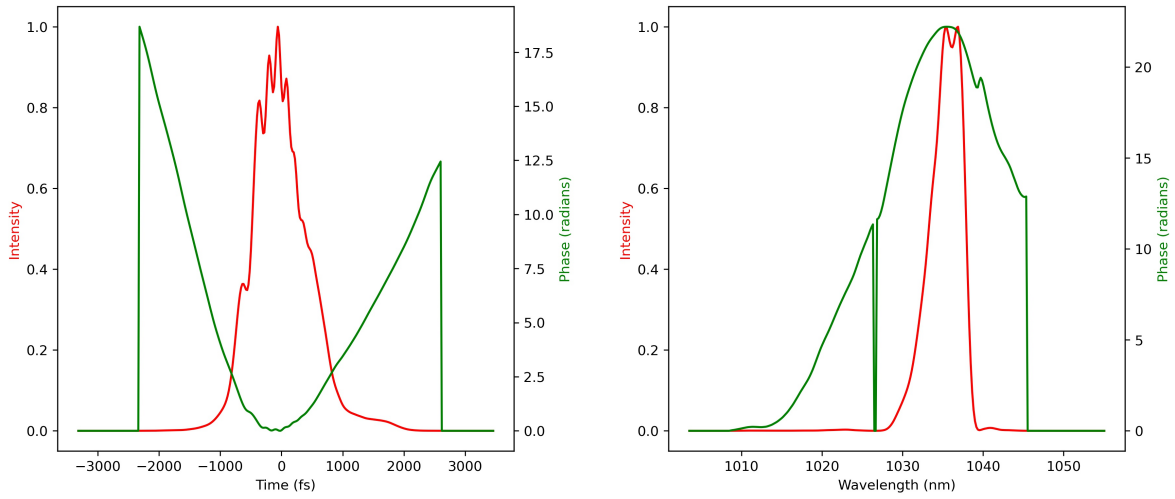

Figure 4.9: Retrieved pulse and phase (left), retrieved spectrum and spectral phase (right) using Femtosoft

We thus reach a pulse width of 862.6 fs, well in accordance with what we expected it to be. This time however, it diverges more from the autocorrelation method by 22.8%. This can be explained by the

Table 4.6: Retrieved amplifier pulse parameters

Autocorrelation FWHM	1442 fs
Temporal FWHM	862.6 fs
FWHM TBWP	1.123
Error	0.003

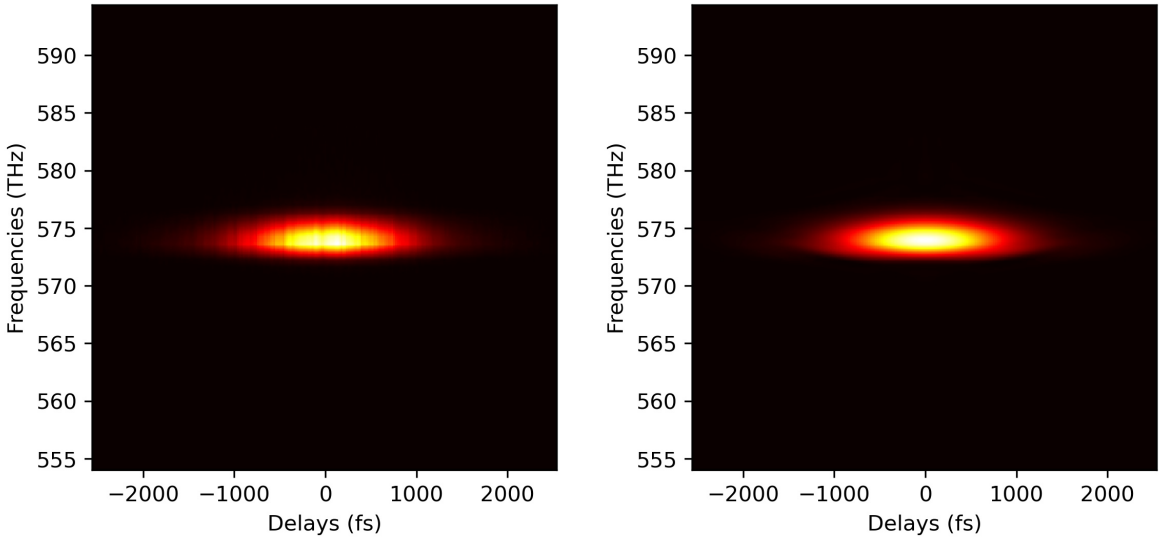

Figure 4.10: Visual comparison between the retrieved (right) and original (retrieved) Yb:YAG InnoSlab amplifier FROG trace

shape of the pulse being less Gaussian as shown in figure 4.9. Indeed the TBWP differs from that of a Gaussian by a lot this time, standing at 1.123 in comparison with the Gaussians' 0.44.

Regarding the phase, a linear chirp can be observed, but again, we have to be skeptic about that.

4.2.3 Ptychographic algorithm

We applied again the algorithm, obtaining the results presented in figure 4.11. The retrieval was more successful than the previous with an error of 0.0623. This time, the spectrum was stretched a little more in comparison with the delays, which explains the lower error.

Figure 4.12 shows the pulse and phase and a recovered value of 875.9 fs. A Gaussian was fitted, but this time, it does not fit as well as in the previous example. The interval this value admits given the error is [821.3 , 930.5] fs, which includes the 862.6 fs previously found, and so we will take the previous value as the correct one. For the same reason than before, we deem this phase to be more trustworthy.

4.3 Fastlite mid-infrared OPCPA

We finally come to the laser that motivated this work. Table 4.7 presents its relevant characteristics. The wavelength range is now in the mid-infrared. Since the beamsplitter already installed was not suitable for this range, it had to be changed along with the nonlinear crystal.

The overlap interval in the translation stage was of $d = c \cdot t/2 = 6$ µm.

We scanned the delay stage with a photo diode in steps of 0.5 fs, over a range of 220 ps, corresponding to 440 points of delay with a step size of 0.075 µm.

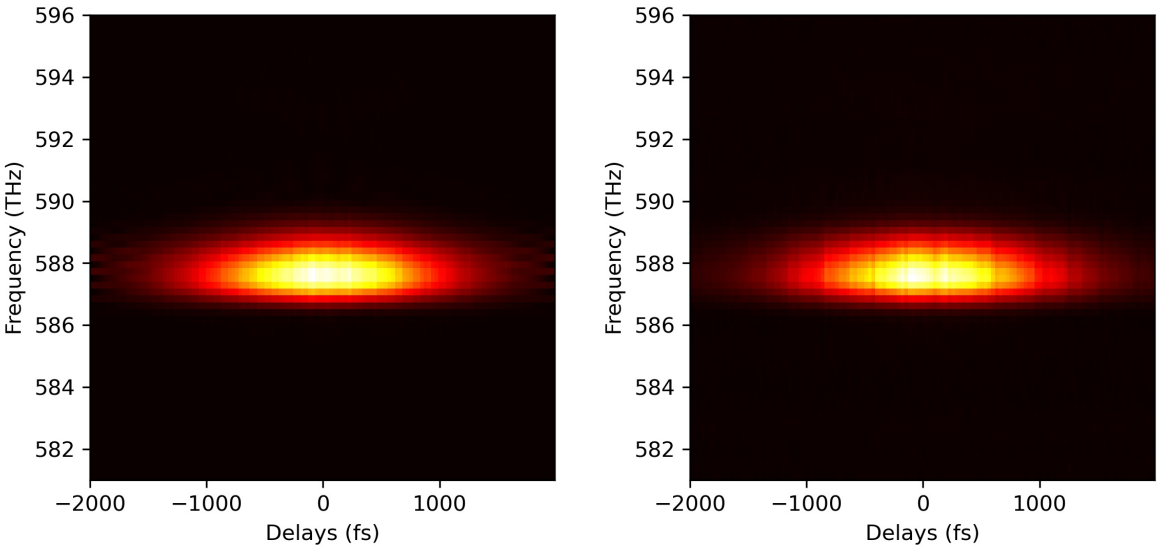

Figure 4.11: Original (left) and retrieved (right) amplifier FROG traces using the ptychographic algorithm

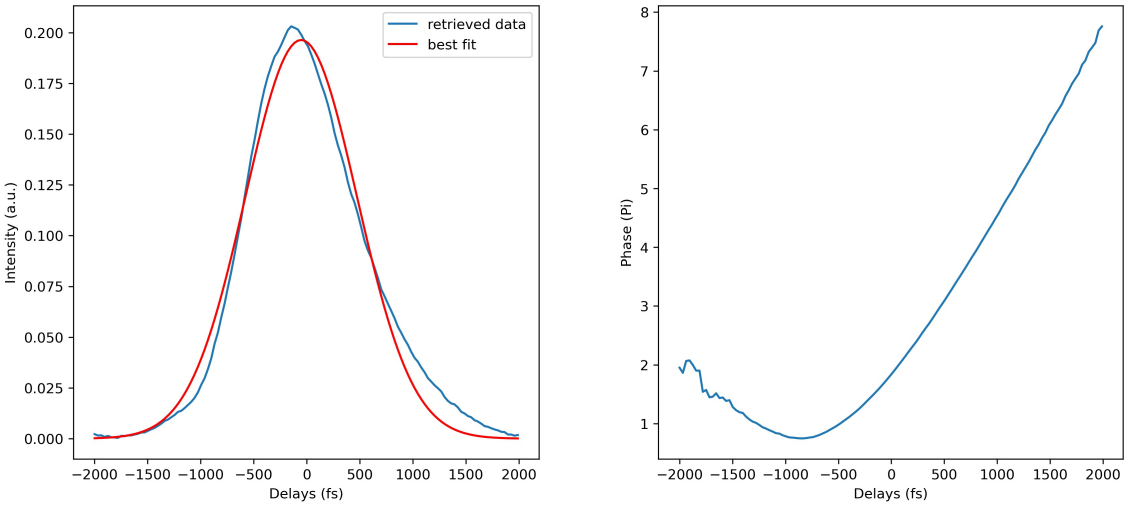

Figure 4.12: Retrieved amplifier pulse (left) and phase (right) using the ptychographic algorithm

We now used the autocorrelation LabVIEW program since we were not able to obtain the spectrogram.

Figure 4.13 shows the the data retrieved, and the best Gaussian fit. The irregular data in peak hints that the pulse is not so well behaved, although it could also be due to some fluctuations in the air, temperature, humidity or illumination. Nevertheless, the FWHM of the fit is of 46 fs, and applying the Gaussian form factor, we retrieve 46/1.414 = 33 fs. It is definitely in the range that we were expecting, and, in that sense, we can say the device worked properly. However we cannot evaluate by how much the measurement is off due to our uncertainty regarding the pulse shape. As we saw in the previous sections, this can alter the result by at least 22.8% for the case of the Amphos amplifier. This represents an interval between [24.2 ; 40.5] fs, which includes the 40 fs that we were anticipating. However, if the irregularities in the peak are not an error in the data acquisition, they suggests that the pulse might have several peaks, and, as such, the Gaussian does not go as high because it averages out all the values into one single peak. Should that be the case then the pulse is wider and fits more in the neighborhood of 40 fs. But this remains a highly qualitative analysis.

Table 4.7: Fastlite mid-infrared OPCPA laser parameters

Repetition rate	100 kHz
Pulse energy	60 µJ
Wavelength	3000 nm
Pulse length	≈ 40 fs

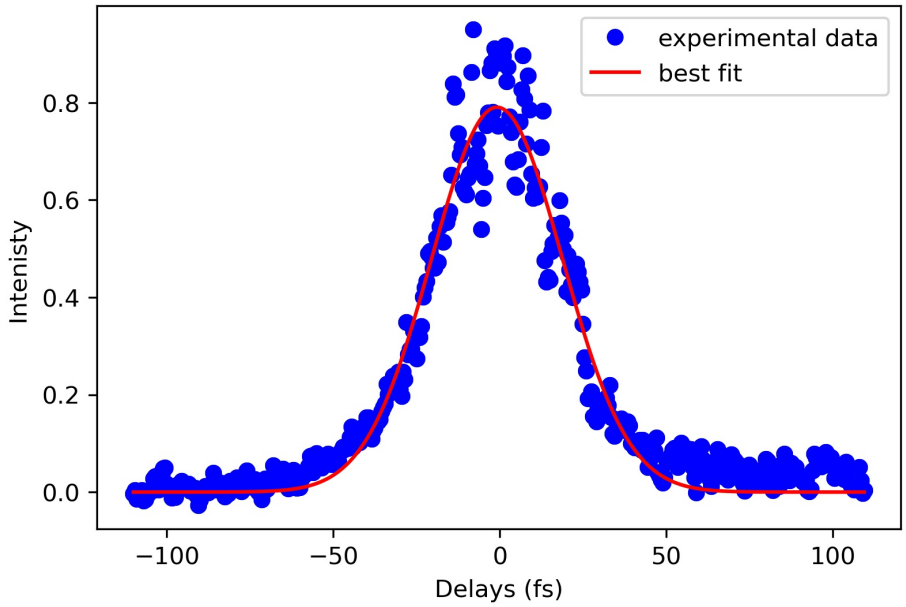

Figure 4.13: Gaussian fit of the Fastlite autocorrelation

In closing, we have characterized three pulses in this chapter. The 1 µm coherent mira Ti:sapphire oscillator has a pulse width of 188.2 fs, and the 1 µm amphos Yb:YAG InnoSlab amplifier 862.6 fs. Both of these were determined with a high level of certainty with the reliable FROG techniques. The third was the 3 µm Fastlite mid-infrared OPCPA, which yielded 33 fs with the less precise autocorrelation technique.

Chapter 5

Conclusions and perspectives

We have described in this work how we planned a frequency resolved optical gating diagnostic for the calculation of the temporal shape and spectral phase of a 3 µm mid-infrared laser. In particular, we tested a SHG-FROG recovery algorithm of ptychographic nature in the hope of achieving superior exactitude in the measurement.

We explored the difficulties of the characterization of pulses in this wavelength range and proposed a design optimized to tackle each of the difficulties. Specifically, we showed why the $AgGaS_2$ was the best choice for our application.

We detailed how the design evolved into the final product, and how the data acquisition was controlled.

We characterized, with great precision thanks to the FROG technique, two 1 µm lasers, the coherent mira Ti:sapphireoscillator and the amphos Yb:YAG InnoSlab amplifier, obtaining a pulse width of 188.2 fs for the first, and 862.6 fs for the latter. With less precision, we obtained a pulse width of 33 fs for the 3 µm fastlight mid-infrared OPCPA using the autocorrelation method.

To improve on this work, a spectrometer with a higher resolution could be used in order to have a more detailed spectrum for the ptychographic algorithm in particular. For a more precise characterization with FROG of the 3 µm pulse the photodiode can be replaced by a spectrometer.

Yet this is but the foundation on which future research in the Laboratory for Intense Lasers will be built on. We now have a greater confidence on the length of the pulse, which in turn allows for more meaningful research in the domain of ultrafast optics.

Bibliography

[1] Saleh Bahaa E. A. and Malvin Carl Teich. “Fundamentals of Photonics 3rd Edition”. In: 5 (2013), pp. 1078–1159. ISSN: 978-1-84872-071-8 (Paperback); 978-1-84872-070-1 (Hardcover). URL: https://www.crcpress.com/Fundamentals-of-Picoscience/Sattler/p/book/9781466505094{\#}googlePreviewContainer.

[2] Sabine Keiber et al. “Electro-optic sampling of near-infrared waveforms”. In: *Nature Photonics* 10.3 (2016), pp. 159–162. ISSN: 17494893. DOI: 10.1038/nphoton.2015.269.

[3] Pamela Bowlan et al. “Measuring the spatiotemporal electric field of ultrashort pulses with high spatial and spectral resolution”. In: *Journal of the Optical Society of America B* 25.6 (2008), A81. ISSN: 0740-3224. DOI: 10.1364/josab.25.000a81.

[4] Edwin J. Akutowicz. “On the determination of the phase of a Fourier integral. I”. In: *Transactions of the American Mathematical Society* (1956). ISSN: 0002-9947. DOI: 10.1090/s0002-9947-1956-0080802-2.

[5] Edwin J. Akutowicz. “On the Determination of the Phase of a Fourier Integral, II”. In: *Proceedings of the American Mathematical Society* (1957). ISSN: 00029939. DOI: 10.2307/2033718.

[6] R. Trebino et al. “Highly reliable measurement of ultrashort laser pulses”. In: *Journal of Applied Physics* 128.17 (2020). ISSN: 10897550. DOI: 10.1063/5.0022552.

[7] Daniel J. Kane and Rick Trebino. “Characterization of Arbitrary Femtosecond Pulses Using Frequency-Resolved Optical Gating”. In: *IEEE Journal of Quantum Electronics* 29.2 (1993), pp. 571–579. DOI: 10.1109/3.199311.

[8] Daniel J. Kane and Rick Trebino. “Single-shot measurement of the intensity and phase of an arbitrary ultrashort pulse by using frequency-resolved optical gating”. In: *Optics Letters, Vol. 18, Issue 10, pp. 823-825* 18.10 (1993), pp. 823–825. ISSN: 1539-4794. DOI: 10.1364/OL.18.000823. URL: https://www.osapublishing.org/viewmedia.cfm?uri=ol-18-10-823{\&}seq=0{\&}html=truehttps://www.osapublishing.org/abstract.cfm?uri=ol-18-10-823https://www.osapublishing.org/ol/abstract.cfm?uri=ol-18-10-823.

[9] Rick Trebino. “Frequency-Resolved Optical Gating: The Measurement of Ultrashort Laser Pulses”. In: *Frequency-Resolved Optical Gating: The Measurement of Ultrashort Laser Pulses* (2000), pp. 1–88. DOI: 10.1007/978-1-4615-1181-6.

[10] Pavel Sidorenko et al. “Ptychographic reconstruction algorithm for FROG: Supreme robustness and super-resolution”. In: *2016 Conference on Lasers and Electro-Optics, CLEO 2016* 3.12 (2016). DOI: 10.1364/cleo_si.2016.stu4i.3.

[11] Rana Jafari, Rick Trebino, and Travis Jones. “100% reliable algorithm for second-harmonic-generation frequency-resolved optical gating”. In: *Optics Express, Vol. 27, Issue 3, pp. 2112-2124* 27.3 (2019), pp. 2112–2124. ISSN: 1094-4087. DOI: 10.1364/OE.27.002112. URL: https://www.osapublishing.org/viewmedia.cfm?uri=oe-27-3-2112{\&}seq=0{\&}html=truehttps://www.osapublishing.org/abstract.cfm?uri=oe-27-3-2112https://www.osapublishing.org/oe/abstract.cfm?uri=oe-27-3-2112.

[12] Rana Jafari and Rick Trebino. “Highly Reliable Frequency-Resolved Optical Gating Pulse-Retrieval Algorithmic Approach”. In: *IEEE Journal of Quantum Electronics* 55.4 (2019). DOI: 10.1109/JQE.2019.2920670.

[13] Rana Jafari and Rick Trebino. “Extremely Robust Pulse Retrieval from even Noisy Second-Harmonic-Generation Frequency-Resolved Optical Gating Traces”. In: *IEEE Journal of Quantum Electronics* 56.1 (2020). DOI: 10.1109/JQE.2019.2950458.

[14] P. K. Bates, O. Chalus, and J. Biegert. “Ultrashort pulse characterization in the mid-infrared”. In: *Optics Letters* 35.9 (2010), p. 1377. ISSN: 0146-9592. DOI: 10.1364/ol.35.001377.

[15] K. Michelmann et al. “Frequency resolved optical gating in the UV using the electronic Kerr effect”. In: *Applied Physics B: Lasers and Optics* 63.5 (1996), pp. 485–489. ISSN: 09462171. DOI: 10.1007/BF01828945.

[16] J. Hunter et al. “Frequency-resolved optical gating with the use of second-harmonic generation”. In: *JOSA B, Vol. 11, Issue 11, pp. 2206-2215* 11.11 (1994), pp. 2206–2215. ISSN: 1520-8540. DOI: 10.1364/JOSAB.11.002206. URL: https://www.osapublishing.org/viewmedia.cfm?uri=josab-11-11-2206{\&}seq=0{\&}html=truehttps://www.osapublishing.org/abstract.cfm?uri=josab-11-11-2206https://www.osapublishing.org/josab/abstract.cfm?uri=josab-11-11-2206.

[17] B. A. Richman, M. A. Krumbügel, and R. Trebino. “Temporal characterization of mid-IR free-electron-laser pulses by frequency-resolved optical gating”. In: *Optics Letters, Vol. 22, Issue 10, pp. 721-723* 22.10 (1997), pp. 721–723. ISSN: 1539-4794. DOI: 10.1364/OL.22.000721. URL: https://www.osapublishing.org/viewmedia.cfm?uri=ol-22-10-721{\&}seq=0{\&}html=truehttps://www.osapublishing.org/abstract.cfm?uri=ol-22-10-721https://www.osapublishing.org/ol/abstract.cfm?uri=ol-22-10-721.

[18] Ivan Amat-Roldn et al. “Ultrashort pulse characterisation with SHG collinear-FROG”. In: *Optics Express* 12.6 (2004), p. 1169. ISSN: 1094-4087. DOI: 10.1364/opex.12.001169.

[19] *SNLO (free version) - AS-Photonics*. URL: https://as-photonics.com/products/snlo/ (visited on 10/29/2021).

Appendix A

Labview block diagrams

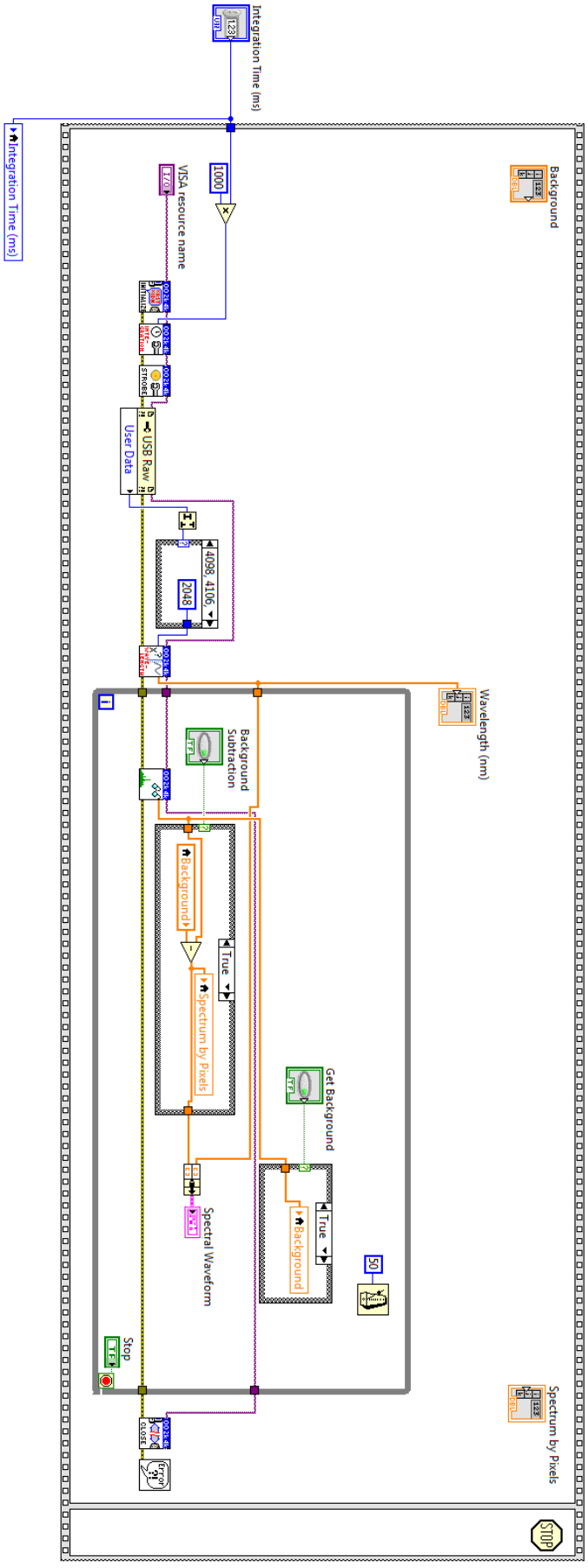

Figure A.1: LabVIEW spectrometer block diagram

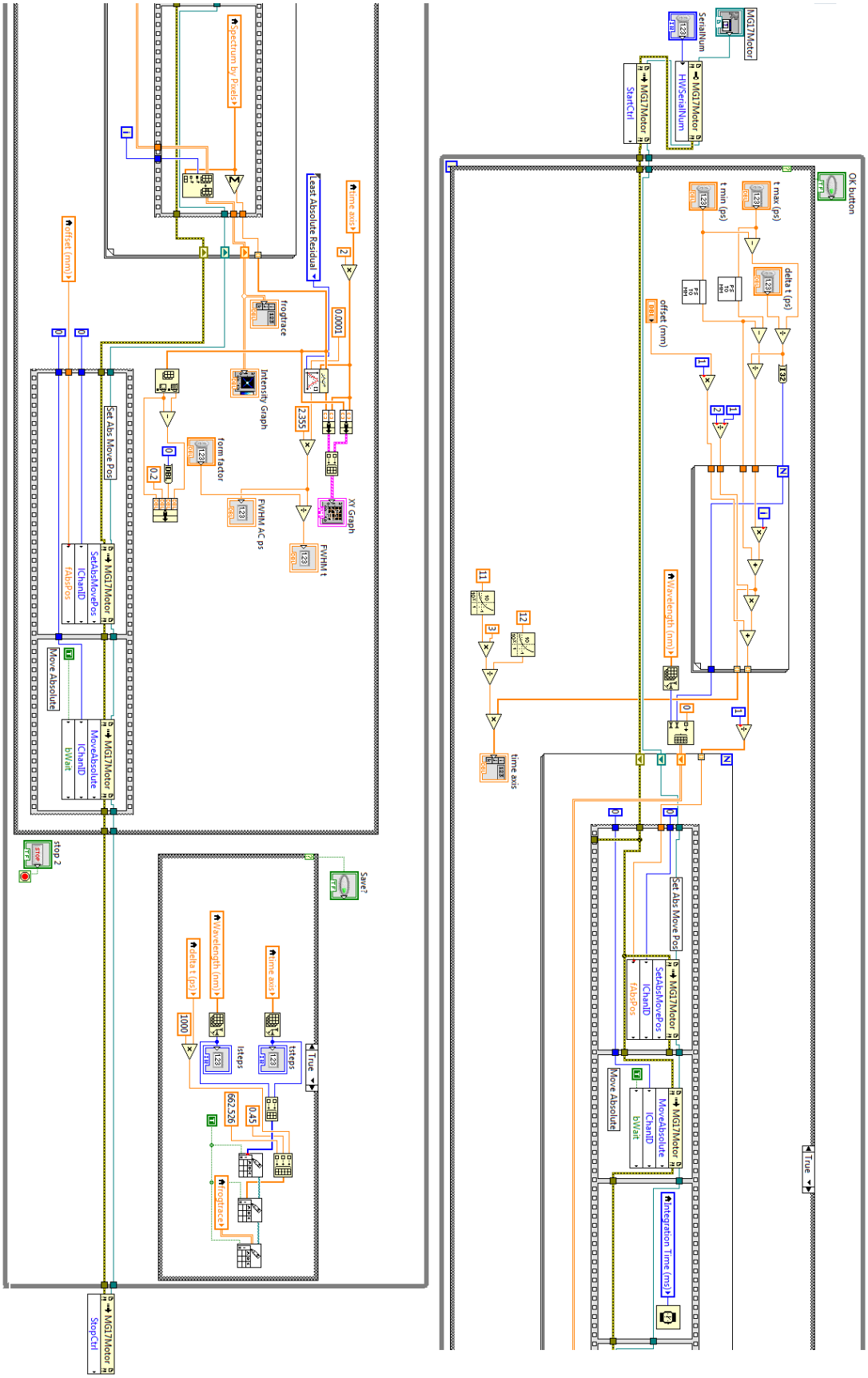

Figure A.2: LabVIEW motor and acquisition block diagram

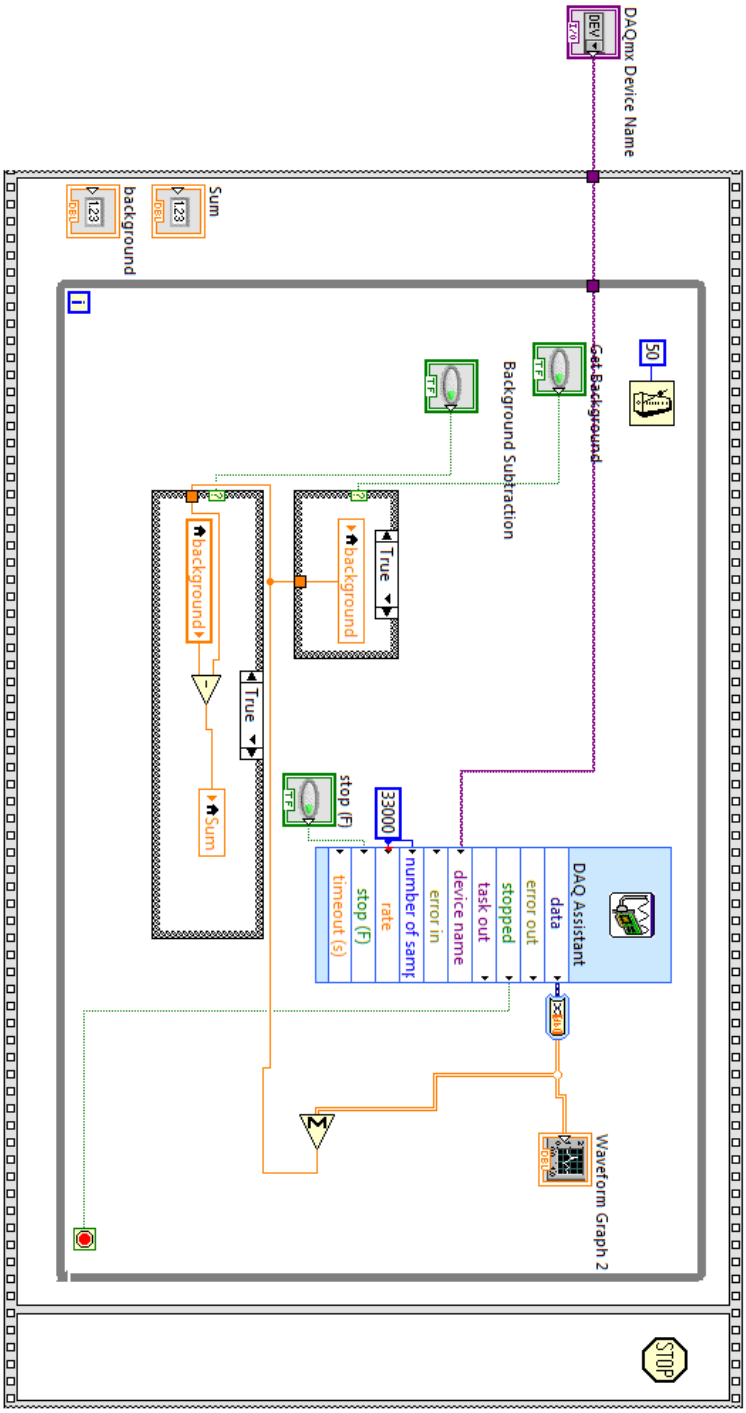

Figure A.3: LabVIEW photodiode

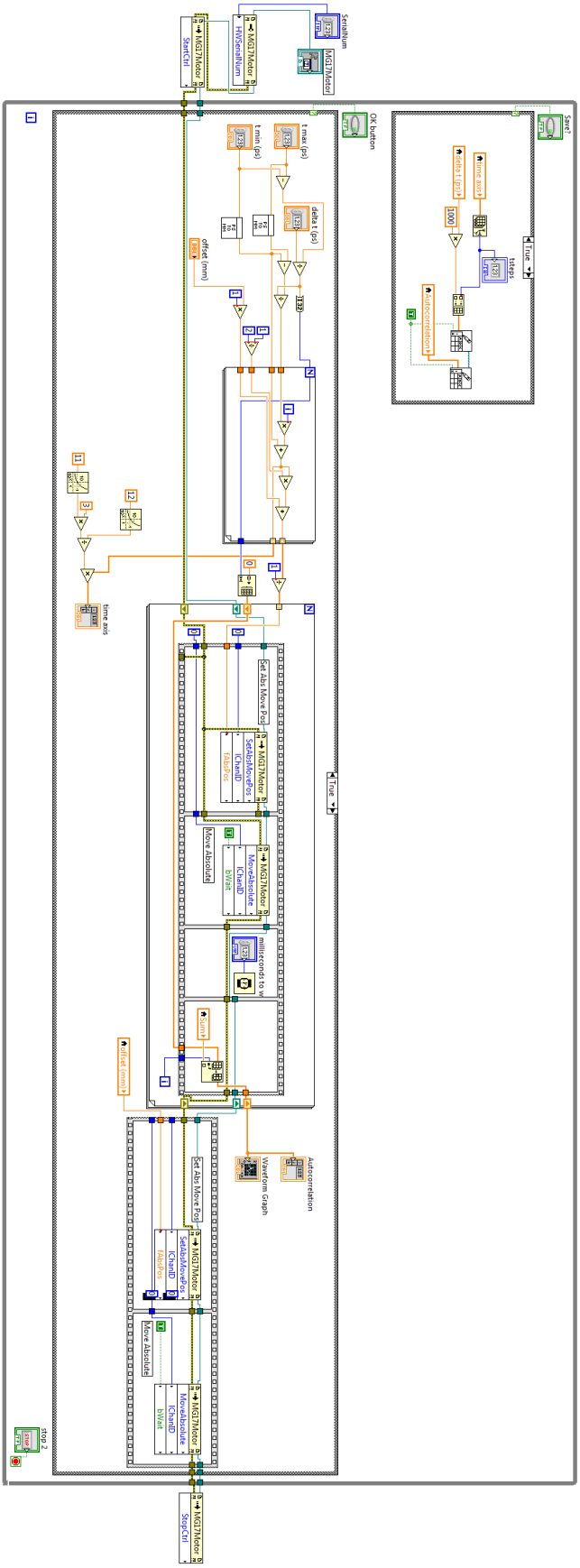

Figure A.4: LabVIEW autocorrelation and acquistion block diagram